Scuola di
Scienze Matematiche
Fisiche e Naturali
Corso di Laurea Magistrale
Scienze Fisiche e Astrofisiche

Realization and characterization of a 425.5nm laser source for ^{53}Cr atoms cooling obtained via second harmonic generation.

Relatore:
Dott. **Matteo Zaccanti**

Correlatore:
Prof. **Massimo Inguscio**

Candidato:
Francesco-Savino Di Noia

Anno Accademico: 2015/2016

Alla mia famiglia
e a Carmen

Contents

Introduction

At temperatures near absolute zero, the quantum nature of particles becomes apparent, leading to fascinating phenomena which can be observed and investigated in nowadays experiments of ultracold atomic gases.
A key feature of quantum gases is the ultimate ability to experimentally control all relevant system parameters, firstly the inter-particle interaction. This allows to study and unveil with unprecedented precision a wealth of complex phenomena that share similarities and interesting inter-connections with other research fields like high-temperature superconductivity [14], quantum chemistry [15], condensed matter [16] and few-body physics [17]. This has lead in recent years to a much cross-fertilization between these various fields.
The achievement of the first Bose-Einstein condensation in 1995 has marked the beginning of a rapid growth in the field of ultracold quantum gases [18, 19, 20]. A further important development has been the cooling of atomic Fermi gases well below the degeneracy temperature, both via direct evaporative cooling of a two-fermion mixture [8, 13] and via sympathetic cooling with a bosonic species [9, 21, 6].
The vast majority of ultracold gases experiments performed so far employ elements from the alkali series. These atomic species are appealing for their simplicity both from the theoretical and experimental point of view: from the theoretical side, they exhibit simple, isotropic short-range interaction that allows for the quantum simulation of a variety of many-body hamiltonians [7, 10]. Furthermore and very importantly, from the experimental point of view their simple energy level structure provides suitable optical

transitions for the implementation of laser cooling schemes, that are easily accessible with the exploitation of relatively unexpensive diode laser sources. The impressive progresses made in cooling and trapping alkali atoms have stimulated studies on more exotic species, such as Cr [22, 23], Yb [5], Sr [24, 25], Ca [26], and more recently Dy [27] and Er [28]. Two (rather than one) valence electrons species exhibit a rich electronic structure of singlet and triplet states, connected by narrow intercombination lines. Such transitions of mHz-width are appealing in optical clock experiments and for metrological applications, and the unique properties of these elements set the basis of recently proposed schemes of quantum simulation, especially targeted at the investigation of quantum magnetism and spin models. Moreover, atomic species such as Cr, Er and Dy, which exhibit a large magnetic dipole moment, have opened the route for the investigation of many-body physics dominated by long-ranged, anisotropic dipole-dipole interaction, which allows to explore qualitatively new phenomena in quantum systems.

However, from the experimental point of view, bringing to quantum degeneracy non-alkali atoms represents a challenge. Because of their complex electronic structure, these species exhibit a wide variety of optical transitions, whose natural linewidth spans from few tens of MHz down to mHz. Furthermore, often the wavelength of the light required for laser cooling these atomic species falls in the blue region of the optical spectrum, for which high-power laser diodes are not available yet. Hence, usually such species require rather expensive laser sources (such as Ti:Sapphire lasers) that are subsequently frequency doubled by non-linear crystals.

In this thesis, we designed, developed and characterized an unexpensive and conceptually simple 425.5 nm blue laser source. Our setup consists of a commercial diode laser that injects a home-made tapered amplifier able to deliver up to 3 Watts of infrared light at 851 nm; this is successively frequency doubled by a non-linear crystal placed inside a home-built optical cavity. In the near future, we will employ such a blue light source for laser cooling of Chromium atoms. Importantly, our simple and easy-to-handle system can be equally well employed for cooling and manipulating other atomic species such as Sr, Ca, Er, Dy, and also Yb.

This thesis is structured as follows. In Chap.1 we discuss the theoretical basis of the Second Harmonic Generation. Chapter 2 explains our frequency doubling cavity design. Chapter 3 describes the optical setup employed to amplify our master laser light and to incouple it in an optical fiber. In Chap. 4 the optical setup needed for creation of the cooling light is explained as well as details of our locking technique. Chapter 5 shows the results obtained for our generated 425.5nm light. Finally, we conclude giving a short outlook on the future developments and possible improvements of our setup.

Chapter 1

Nonlinear Optics

In this chapter we give a theoretical description of the second harmonic generation (SHG) process. In section 1.1 we explain how a second order polarization in non-centrosymmetric media under strong optical fields acts like a source of second harmonic radiation. In section 1.2 we show how this phenomenon critically depends on the relation between the wavevector of the incident and the second harmonic field. We will see then how to evaluate the efficiency of the SHG process in a plane wave approach and in the physically relevant case of Gaussian beams (sect. 1.3), and in section 1.4 we discuss how we choose the nonlinear crystals for our experiment.

1.1 Second Harmonic Generation Theory

The interaction between a dielectric medium and an incoming light radiation is generally described by the relation between the induced polarization density $\vec{P}$ of the medium and the incident electric field $\vec{E}$.
Linear optics considers the case in which this relation is linear, and given by:

$$\vec{P} = \varepsilon_0 \chi \vec{E} \tag{1.1}$$

where ε_0 is the permittivity of free space and χ is the electric susceptibility of the medium. In writing this equation we have assumed that the medium is non-dispersive, homogeneous and isotropic. Under these assumptions the vectors $\vec{P}$ and $\vec{E}$ are parallel at each space and time position, and we

can therefore treat them on a component-by-component basis (the so called "scalar approximation").
The electric displacement field is given by $\vec{D} = \varepsilon_0\vec{E} + \vec{P} = \varepsilon_0(1+\chi)\vec{E}$; the fields in the medium are related by the Maxwell's equations:

$$\begin{cases} \vec{\nabla}\cdot\vec{D} = 0 \\ \vec{\nabla}\times\vec{E} = -\frac{\partial\vec{B}}{\partial t} \\ \vec{\nabla}\cdot\vec{B} = 0 \\ \vec{\nabla}\times\vec{H} = \frac{\partial\vec{D}}{\partial t} \end{cases} \tag{1.2}$$

The quantity $1+\chi$ is the relative dielectric constant ε_r, so the displacement field can also be expressed as $\vec{D} = \varepsilon_0\varepsilon_r\vec{E} = \varepsilon\vec{E}$.

A nonlinear dielectric medium, on the other hand, is characterized by a nonlinear relation between $\vec{P}$ and $\vec{E}$. For a first understanding of this nonlinear behaviour we briefly consider the Lorentz model [36], which describes the atom as a harmonic oscillator. The electrons interact with the nucleus with spring-like forces, and the equation of motion of each electron under an external electric field is given by[1]:

$$\ddot{x} + \gamma\dot{x} + \omega_0^2 x = -eE/m \tag{1.3}$$

where we have considered a damping force of the form $\gamma m\dot{x}$, coming from internal collisions in the solid and radiation emission, and we have taken $\vec{E} \parallel \vec{x}$; ω_0 is the characteristic frequency of the electron.
Solving this equation for the case of a monochromatic field $E(t) = Ee^{i\omega t}$ we find the well known expression for the electron displacement from its equilibrium position due to the electric field:

$$x(t) = \frac{-e}{m}\frac{1}{(\omega_0^2 - \omega^2) + i\omega\gamma}E(t) \tag{1.4}$$

If we denote with N the number density of dipoles, the expression of the

[1]This treatment can be extended to the ions in a crystal, replacing the mass and the charge of the electron with the ion's ones.

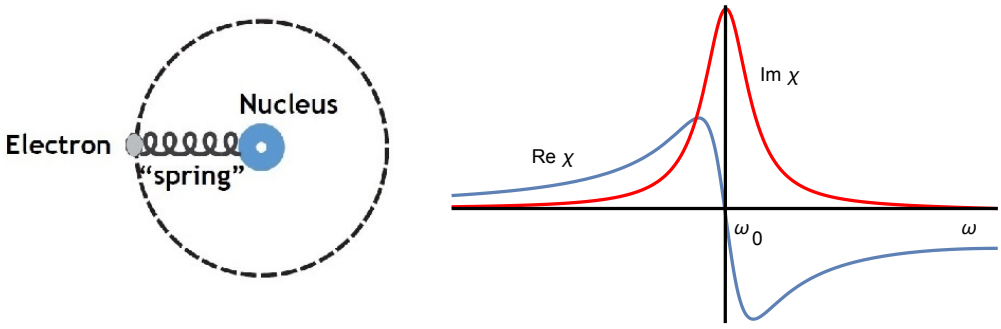

Figure 1.1: Lorentz model of the atom; the imaginary part of χ is responsible of media absorptions.

(linear) polarization density P (1.1) reads:

$$P = -eNx = \frac{Ne^2}{m}\frac{1}{(\omega_0^2 - \omega^2) + i\omega\gamma}E = \epsilon_0\chi E \tag{1.5}$$

The dependence of χ on ω is illustrated in Figure 1.1. The time dependence of P resides in E; the induced dipoles will then oscillate at the same frequency as the electric field E.

Let us see now what happens if we introduce an additional term of the form ax^2 in the equation of motion, by considering a restoring force of the kind:

$$\vec{F}_{rest} = -m\omega_0^2 x - max^2 \tag{1.6}$$

Now the force is nonlinear in the displacement, and a is a parameter that characterizes the strength of such nonlinearity. Since in real situations usually the non-linear effects are small, we can treat first the ax^2 term as a perturbation. Solving the equation of motion with the perturbation theory, at first order in x we find again the relation (1.5). For the second order we find a displacement (hence a polarization) that is quadratic in E and that oscillates at a frequency that is twice that of the incident field. Namely, for a monochromatic input field of frequency ω we find [2, 3]:

$$x^{(2)} = \frac{-a(q/m)^2E^2}{(\omega_0^2 - \omega^2 - i\omega\gamma)^2(\omega_0^2 - 4\omega^2 - i2\omega\gamma)}e^{-2i\omega t} + const \tag{1.7}$$

As we will see later, this second order term represents the source of second harmonic generation and other related phenomena.

It is possible to estimate the magnitude of the nonlinear coefficient a by noticing that the linear and nonlinear contributions to the restoring force are expected to become comparable when the displacement x of the electron from its equilibrium position is approximately equal to the size of the atom [2]. Equivalently, we can think that nonlinear effects become sizeable when E acquires values comparable to interatomic electric fields, which are typically $\sim 10^5$ - 10^8 V/m. This is the main reason for which nonlinear optics has been experimentally explored only after the invention of laser, which allows to reach such high values of optical fields.
One last important feature that comes out from this model concerns the physical structure of nonlinear media. If we consider the restoring force (1.6) as an x-derivative of the potential acting on the electron, we easily see that a quadratic contribution in the force corresponds to a cubic term in the potential (see Figure 1.2). Such a term is odd with respect to x, so the total potential will no longer be symmetric. Such a potential can exist only in non-centrosymmetric materials[2].

So far we have given a qualitative and intuitive description for the development of a nonlinear polarization. In the following we discuss a more formal approach that will allow us to describe more quantitatively the process of second harmonic generation. We consider the Taylor's expansion of the polarization P as a function of E:

$$\begin{aligned} P(t) = P^{(1)}(t) + P^{(2)}(t) + P^{(3)}(t) + ... = \\ = \varepsilon_0 \left(\chi^{(1)} E(t) + \chi^{(2)} E^2(t) + \chi^{(3)} E^3(t) + ... \right) \end{aligned} \tag{1.8}$$

where $\chi^{(n)}$ is the n-order susceptibility.

[2]For a centrosymmetric material only even terms are possible in equation (1.8), which can also bring higher order nonlinear phenomena.

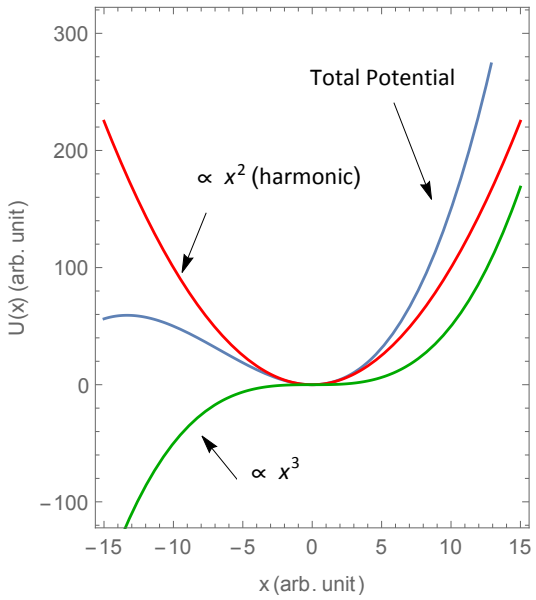

Figure 1.2: Nonlinear potential for a non-centrosymmetric medium.

For an incident field generally composed of two plane waves of frequencies ω_1 and ω_2

$$E(t) = E_1 e^{-i\omega_1 t} + E_2 e^{-i\omega_2 t} + c.c. \tag{1.9}$$

the corresponding second order polarization reads:

$$P^{(2)}(t) = \varepsilon_0 \chi^{(2)} E^2(t) = 2\varepsilon_0 \chi^{(2)}(|E_1|^2 + |E_2|^2) +$$
$$+\varepsilon_0 \chi^{(2)}(|E_1|^2 e^{-i2\omega_1 t} + |E_2|^2 e^{-i2\omega_2 t} + 2E_1 E_2^* e^{-i(\omega_1+\omega_2)t} + 2E_1^* E_2 e^{-i(\omega_2-\omega_1)t} + c.c.) \tag{1.10}$$

Here we can distinguish three different components:

- a term that is constant in time.
- two terms oscillating with frequencies given by the double of the incident frequencies.
- two terms oscillating with a frequency given by the sum and by the difference of the incident frequencies, respectively.

Each of these components can be regarded as a source of radiation at these frequencies.

In fact, by combining Maxwell's equations (1.2) we can get the well known wave equation:

$$\vec{\nabla}^2\vec{E}_n - \frac{\varepsilon_r(\omega_n)}{c^2}\frac{\partial\vec{E}_n}{\partial t^2} = \frac{1}{\varepsilon_0 c^2}\frac{\partial^2\vec{P}_n}{\partial^2 t} \tag{1.11}$$

where the n index stands for different frequency components. From here we can see that the various components of the non linear polarization term (1.10) act like sources of electrical fields with $\omega = \omega_n$.

We release now some of the assumptions we made. In particular we consider the case of a non isotropic medium. This will complicate the formalism, but will allow us to treat the physically relevant case of non-centrosymmetric media. Indeed, we will see that for second harmonic generation we need to exploit birefringence, a feature peculiar of some non isotropic crystals. In this more general case, we cannot use the scalar approximation anymore and the susceptibility will be no longer a scalar quantity. Namely, it will be a vector with generally three different i, j, k components along the three spatial directions. Consequently Eq. (1.8) reads in this case as:

$$P_i(t) = \varepsilon_0 \sum_j \chi^{(1)}_{ij} E_j + \varepsilon_0 \sum_{jk} \chi^{(2)}_{ijk} E_j E_k + ... \tag{1.12}$$

In the most general case, we assume that we can represent both the electric field of the incident wave and the medium polarization as the discrete sum of a number of frequency components as:

$$\vec{E}(\vec{r},t) = \sum_n \vec{E}(\omega_n)e^{-i\omega_n t} \tag{1.13}$$

$$\vec{P}(\vec{r},t) = \sum_n \vec{P}(\omega_n)e^{-i\omega_n t} \tag{1.14}$$

We define then the various elements of the second order susceptibility tensor $\chi^{(2)}_{ijk}$ as the constants of proportionality relating the amplitude of the nonlinear polarization to the product of field amplitudes according to

$$P^{(2)}_i(\omega_n + \omega_m) = \varepsilon_0 \sum_{jk} \sum_{(nm)} \chi^{(2)}_{ijk}(\omega_n + \omega_m) E_j(\omega_n) E_k(\omega_m) \tag{1.15}$$

The notation (nm) indicates that, in performing the summation over n and m, the sum $\omega_n + \omega_m$ is to be held fixed, although the single ω_n and ω_m are allowed to vary.
Let us now focus on the second harmonic generation (SHG). In this case we consider the mixing of two frequency components of the same monochromatic wave with frequency ω_1, which generates a field with frequency $\omega_2 = 2\omega_1$. We obtain from (1.15):

$$P_i^{(2)}(\omega_2) = 2\varepsilon_o \sum_{jk} d_{ijk}(\omega_2 = \omega_1 + \omega_1) E_j(\omega_1) E_k(\omega_1) \tag{1.16}$$

where we introduced the nonlinear coefficients:

$$d_{ijk} = \frac{1}{2}\chi_{ijk}^{(2)} \tag{1.17}$$

It can be shown [2] that considering the symmetries of χ_{ijk}, the nonlinear coefficients tensor d_{ijk} can be contracted into a 3×6 matrix d_{ij}, and that for fixed directions of propagation and polarization we can equivalently use a scalar relation for the nonlinear polarization:

$$P^{(2)}(\omega_2) = 2\varepsilon_0 d_{eff} E^2(\omega_1) \tag{1.18}$$

where d_{eff} is the "effective nonlinear coefficient" that can be calculated given d_{ij}, the incident field polarization direction and the material dispersions [35]. For most crystals one can find in literature and directly from the manufacturers simple formulas for calculating d_{eff} from the angle of propagation and the incident field polarization direction [33].

1.2 Phase Matching

As we have seen, because of nonlinearities in the atomic response, each atom of a nonlinear medium develops an oscillating dipole moment which contains a component at frequency $2\omega_1$ ("second harmonic wave"), when interacting with a strong driving field of frequency ω_1 ("fundamental wave"). In our case we will deal with an infrared laser exciting a dipole moment which will emit in the blue. The driving laser light ensures that atoms at different

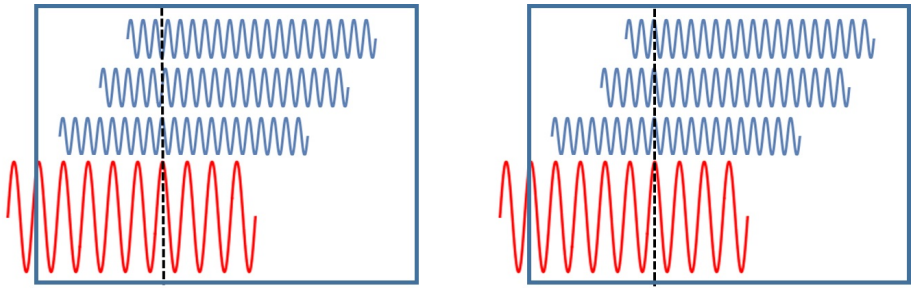

Figure 1.3: Simple phase matching scheme: on the left the dipoles generating second harmonic light at different positions are not in phase; on the right they are in phase and each blue wave will interfere constructively with the others.

positions absorb and emit infrared light in phase with respect to each other. However, this in general is not the case for the second harmonic light: the blue light emitted further along the path inside the nonlinear medium is not necessarily in phase with the blue light already emitted. We want then to find a condition for which the phase is the same for the fundamental and the second harmonic wave, in which case also the blue light adds constructively inside the medium.

We consider now the incident wave as a plane wave propagating in the z direction and fullfilling the Slow Varying Envelope Approximation (i.e. we take $\left|k\frac{\partial E_n}{\partial z}\right| \gg \left|\frac{\partial^2 E_n}{\partial z^2}\right|$). Assuming the collinear case ($\vec{k_1} \parallel \vec{k_2}$), we obtain from the wave equation (1.11):

$$\frac{dE(\omega_2, z)}{dz} = \frac{i\omega_2^2 d_{eff}}{k_2 c^2} |E(\omega_1, z)|^2 e^{i\Delta k z} \tag{1.19}$$

Here $k_{1,2} = \frac{n(\omega_{1,2})\omega_{1,2}}{c}$ are the wavevectors of the fundamental and the SHG waves inside the medium and Δk represents the wavevector "mismatch" $\Delta k = 2k_1 - k_2$. We take now the wave as propagating through a crystal of length l (from $z = 0$ to $z = l$). In the low efficiency regime (also called "undepleted pump regime") we can assume the input intensity to be constant during the propagation in the nonlinear medium. In this approximation we obtain that the SHG field equals:

$$E(\omega_2, l) = \frac{\omega_2^2 d_{eff}}{k_2 c^2} |E(\omega_1)|^2 \left[\frac{e^{i\Delta k l} - 1}{\Delta k}\right] \tag{1.20}$$

where we took $E(\omega_2, 0) = 0$, i.e. we assumed that there is no SHG field at the input facet of the crystal. Correspondly, the SHG intensity reads:

$$\begin{aligned} I(\omega_2, l) = \frac{cn(\omega_2)\varepsilon_0}{2}|E(\omega_2, l)|^2 &\propto \omega_2^4 d_{eff}^2 |I(\omega_1)|^2 l^2 sinc^2[\Delta k l/2] \\ &= \omega_2^4 d_{eff}^2 |I(\omega_1)|^2 4 \frac{sin^2[\Delta k l/2]}{(\Delta k)^2} \end{aligned} \tag{1.21}$$

In Figure 1.4 (a) we show the function $sinc^2[\Delta k l/2]$ as a function of Δk for a fixed l; it features a narrow peak at $\Delta k l/2 = 0$, which corresponds to the situation of *perfect phase matching* $\Delta k = 2k_1 - k_2 = 0$. From Eq. (1.21), we see that for perfect phase matching the second harmonic intensity increases quadratically with the interaction length, since $l^2 sinc^2[\Delta k l/2] \to l^2$. In contrast, whenever $\Delta k \neq 0$, $I(\omega_2)$ will feature a sinusoidal behaviour as a function of l, with a maximum amplitude which decreases for increasing Δk (Figure 1.4 (b)). For a fixed $\Delta k \neq 0$ we have in fact:

$$max\left[I(\omega_2, l)\right] \propto \frac{1}{(\Delta k)^2} \tag{1.22}$$

from which we see that the SHG maximum intensity drops lixe $\frac{1}{(\Delta k)^2}$. This is a crucial point for our purpose: in order to have a good conversion efficiency we shall stay as close as possible to the perfect phase matching condition, otherwise the efficiency will rapidly decrease. It is important to note that also for the more physically relevant case of a gaussian-shaped wavefront this trend qualitatively still holds, despite small quantitative differences (see sect. 1.3).

We will analyze the equations (1.19) and (1.21) in more detail in section 1.3. What we want to underline now is an important physical implication of the SHG phase matching condition. If we take the momentum-frequency relation for a photon inside a medium $k = \frac{n(\omega)\omega}{c}$ and we impose $\Delta k = 0$ with $\omega_2 = 2\omega_1$, we find:

$$2\frac{n(\omega_1)\omega_1}{c} = \frac{n(\omega_2)\omega_2}{c} \Rightarrow n(\omega_1) = n(2\omega_1) \tag{1.23}$$

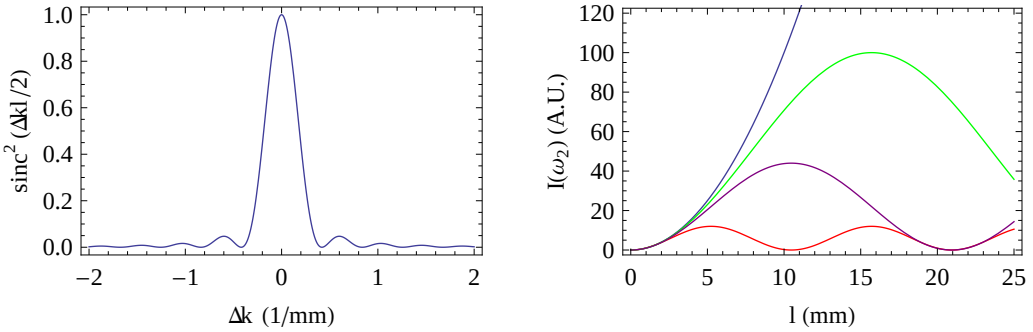

(a) (b)

Figure 1.4: (a): $sinc^2(\Delta kL/2)$ for $l = 15mm$. (b): generated intensity for perfect phase matching (blue), $\Delta k = 0.2mm^{-1} = \Delta k_{FWHM}$ (green), $\Delta k = 0.3mm^{-1}$ (purple), $\Delta k = 0.6mm^{-1}$ (red). We can see the sinusoidal behaviour with decreasing amplitude for increasing Δk explained in the text.

This condition is impossible to reach for an ordinary medium, where the refractive index is a monotonically growing function of ω, as long as there are no absorption lines nearby. Among other possibilities, such as the implementation of quasi phase matching techniques [1], condition (1.23) can be accomplished by exploiting the properties of birefringent crystals.

1.2.1 Birefringent Phase Matching

A light wave travelling through an isotropic medium experiences the same refractive index $n = \sqrt{\varepsilon}$, independently on the propagation direction. In other words, the first order tensor $\varepsilon_{ij} = 1 + \chi_{ij}$ is a diagonal matrix with the same constant for the three spatial directions. This is in general not the case for non-isotropic media, for which ε_{ij} is a non-diagonal matrix. However, in the case of non-absorbing materials, it can be shown that ε_{ij} is always symmetric [1]. Thus, it can be diagonalized with a rotation, that corresponds to the transformation from laboratory reference frame to the *dielectric coordinates system*.

An *uniaxial crystal* in the dielectric coordinates system has a dielectric tensor:

$$\varepsilon_{ij} = \begin{pmatrix} \varepsilon_o & 0 & 0 \\ 0 & \varepsilon_o & 0 \\ 0 & 0 & \varepsilon_e \end{pmatrix} \tag{1.24}$$

This means that in this kind of crystals two of the crystalline axes present the same refractive index $n_o = \sqrt{\varepsilon_o}$, where the "o" stands for "ordinary", while the third axis is called *optic axis* (we choose it as the z axis) and presents an "extraordinary" index $n_e = \sqrt{\varepsilon_e}$. The crystal is said to be positive (negative) if $n_e > n_o$ ($n_e < n_o$).
For a *biaxial crystal* we have:

$$\varepsilon_{ij} = \begin{pmatrix} \varepsilon_x & 0 & 0 \\ 0 & \varepsilon_y & 0 \\ 0 & 0 & \varepsilon_z \end{pmatrix} \tag{1.25}$$

A biaxial crystal exhibits then three different refractive indexes for each crystalline axis. The ordinary/extraordinary and positive/negative distinctions are not so straight-forward for biaxial crystals but similar definitions can be made [35].
We focus for the moment on uniaxial crystals. What we have right now described means physically that a light wave propagating into the crystal will experience a refractive index that depends on its polarization. In Figure 1.5 we schematically sketch the case of an unpolarized wave propagating in the $y - z$ plane inciding on an uniaxial crystal. In the medium we distinguish between the *ordinary wave*, with polarization direction perpendicular to the optic axis, and the *extraordinary wave*, with polarization in the plane containing the wavevector and the optic axis.
We can easily see from the figure that the electric field of an ordinary wave always oscillates along the x axis; the propagation of such a wave is then governed by the normal optics laws of a medium with refractive index n_o.
On the other hand, the electric field of an extraordinary wave will have components both along the y axis and along the optic axis, so we may ask ourselves what is the effective refractive index experienced by the e-wave.

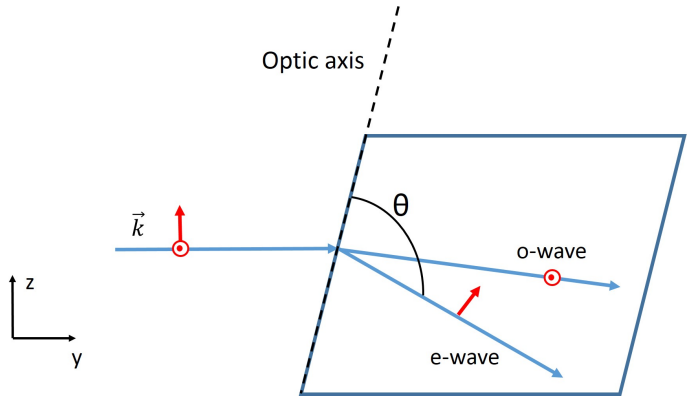

Figure 1.5: An unpolarized wave incident on a positive uniaxial crystal. The ordinary and extraordinary components inside the crystal are separated: this phenomenon is known as "birefringence". In the figure is shown the simple case where the optic axis coincides with one crystal edge.

Solving the wave equation for the extraordinary wave, we find a dispersion relation given by:

$$k^2 \left[\frac{cos^2(\theta)}{n_o^2} + \frac{sin^2(\theta)}{n_e^2} \right] = \frac{\omega^2}{c^2} \tag{1.26}$$

where θ is the angle between $\vec{k}$ and the optic axis (Fig. 1.5); namely, the inverse of the quantity in brackets can be regarded as the square of an angle-dependent refractive index:

$$\frac{1}{n^2(\theta)} = \left[\frac{cos^2(\theta)}{n_o^2} + \frac{sin^2(\theta)}{n_e^2} \right] \tag{1.27}$$

One can easily verify that $n(\theta)$ reduces to n_e for $\theta = \pi/2$ and to n_o for $\theta = 0$, as expected from the definitions. For an e-wave the refractive index can then be "tuned" with θ, by choosing the direction of $\vec{k}$.

This is the key feature which can be exploited to reach the SHG phase matching condition. Because of dispersion the condition (1.23) cannot usually be satisfied, unless the polarization of the fundamental and of the SHG waves is different. For a negative uniaxial crystal the direction at which the wave enters the crystal is adjusted in such a way that $n(\theta, 2\omega_1) = n_o(\omega_1)$, i.e., such that birefringence compensates exactly for dispersion (Figure 1.6). The process is labeled in this case as "o-o-e" since the fundamental beam is an o-wave and the SHG beam is an e-wave. For positive uniaxial crystals we

have instead $n_o(2\omega_1) = n(\theta, \omega_1)$, and the process is labeled as "e-e-o". For biaxial crystals both combinations can be possible, and one will choose the more efficient one.

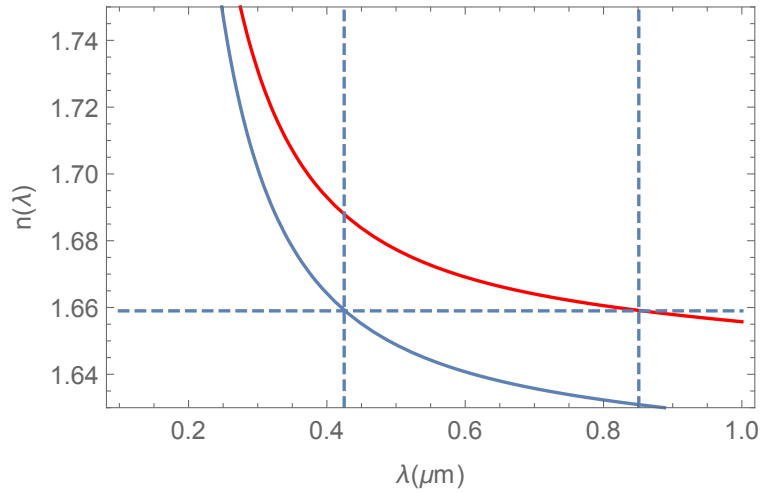

Figure 1.6: Birefringent phase matching for uniaxial BBO crystal. Red line is $n_o(\lambda)$; blue line is $n_e(\lambda)$ for a phase matching angle $\theta = 27.5^o$. The phase matching condition $n_o(\lambda_1) = n_e(\lambda_1/2) = 1.659$ is satisfied for $\lambda_1 = 851nm$.

When we exploit birefringent phase matching we have to take into account an important effect, that is the emergence of a "walkoff" angle between the generated and the incident waves.
In order to understand the origin of this feature, let us consider an incident plane wave $\vec{E} = \vec{E}_0 e^{i(\vec{k}\cdot\vec{r}-\omega t)}$ in an isotropic medium; from Eq. (1.2) we have:

$$\vec{\nabla}\cdot\vec{D} = \varepsilon(\frac{\partial}{\partial x}E_x + \frac{\partial}{\partial y}E_y + \frac{\partial}{\partial z}E_z) = i\varepsilon\vec{k}\cdot\vec{E} = 0 \tag{1.28}$$

Namely, the wavevector $\vec{k}$ is always orthogonal to $\vec{E}$ (these are the so called *transverse waves*).
For a non-isotropic medium, instead, the equation becomes:

$$\vec{\nabla}\cdot\vec{D} = \sum_i \frac{\partial D_i}{\partial x_i} = \sum_i \varepsilon_i \frac{\partial E_i}{\partial x_i} = 0 \Rightarrow \vec{\nabla}\cdot\vec{E} \neq 0 \tag{1.29}$$

where the index i refers to the dielectric coordinates.
The waves are in general no longer transverse; therefore the Poynting vector

$\vec{S} = \vec{E} \times \vec{H}$, associated to the energy flux of the optical wave, will be in general no longer parallel to $\vec{k}$.
This can be easily shown considering an o-wave and an e-wave propagating in an uniaxial crystal with parallel wavevectors, like in the collinear SHG. Let us write $\vec{k}$ in the dielectric coordinates in the vector form:

$$\vec{k} = k(0, sin\theta, cos\theta) \tag{1.30}$$

For the o-wave the electric field $\vec{E}$ will be parallel to x, so we can write $\vec{E}_o = E_o(1, 0, 0)$ and $\vec{D}_o = \varepsilon_o E_o(1, 0, 0)$: in this case the wave is transverse.
For the e-wave the electric field instead will have components both along y and z; in this case it is more convenient to write directly $\vec{D}_e$ using Eq. (1.29), which ensures $\vec{D}_e \perp \vec{k}$, and to exploit the definition of e-wave, which ensures zero component along the x axis. We can then write:

$$\begin{aligned} \vec{D}_e &= D_e(0,\ cos(\theta),\ -sin(\theta)) \\ \Rightarrow \vec{E}_e &= D_e(0,\ \frac{cos(\theta)}{\varepsilon_o},\ -\frac{sin(\theta)}{\varepsilon_e}) \end{aligned} \tag{1.31}$$

This equation shows that $\vec{E}_e$ is not parallel to $\vec{D}_e$; moreover we can easily calculate the expression for $\vec{H}_e$ to be:

$$\begin{aligned} \vec{H}_e &= \frac{cD_e}{n(\theta)}(-1,\ 0,\ 0) \\ \Rightarrow \vec{S}_e = \vec{E}_e \times \vec{H}_e &= \frac{c|D_e|^2}{n(\theta)}(0,\ \frac{sin(\theta)}{\varepsilon_e},\ -\frac{cos(\theta)}{\varepsilon_o}) \end{aligned} \tag{1.32}$$

from which we see that the Poynting Vector is then not parallel to $\vec{k}$; the angle between them is the walkoff angle.
Figure 1.7 summarizes the various relations for the vector quantities of a non-transverse wave; the walkoff angle ρ can be calculated from the refractive indices and angles of propagation through the crystal. What is important for us is the fact that the energy flux of the generated e-wave in the SHG process will propagate with a nonzero angle with respect to the incident wave, and the overlap between them will go to zero after a certain distance. We

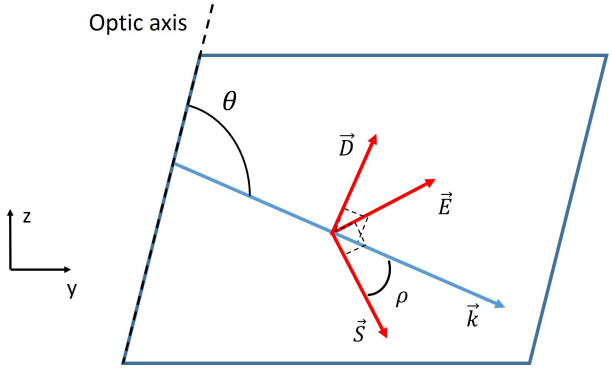

Figure 1.7: Relations between $\vec{E}, \vec{D}, \vec{k}, \vec{S}$ for an e-wave. $\vec{H}$ is in the x direction, outgoing from the yz plane. ρ is the walkoff angle.

will account for this in the SHG efficiency calculations.
The existence of the walkoff angle has another important effect for the experimentally relevant case of gaussian wavefronts. Namely, it leads to a distortion of the beam envelope as shown in Figure 1.8: summing the contribution of different crystal slices to the SHG beam we obtain a beam which has no more a pure Gaussian profile. This effect is stronger for higher ρ, and can lead to quite elongated second harmonic beams (see Chapter 5).
We conclude this section mentioning the case of biaxial crystals. With the convention used in Figure 1.9, we see that both for $\theta = \pi/2, 0$ and for $\phi = \pi/2, 0$, the situation will reduce to the uniaxial crystals case. This is what happens for the biaxial LBO and BIBO crystals that we use in our experiment (see Table 1.1); for intermediate angles, the expression for the refractive index will become more complex, and will exhibit a dependence both in θ and ϕ.

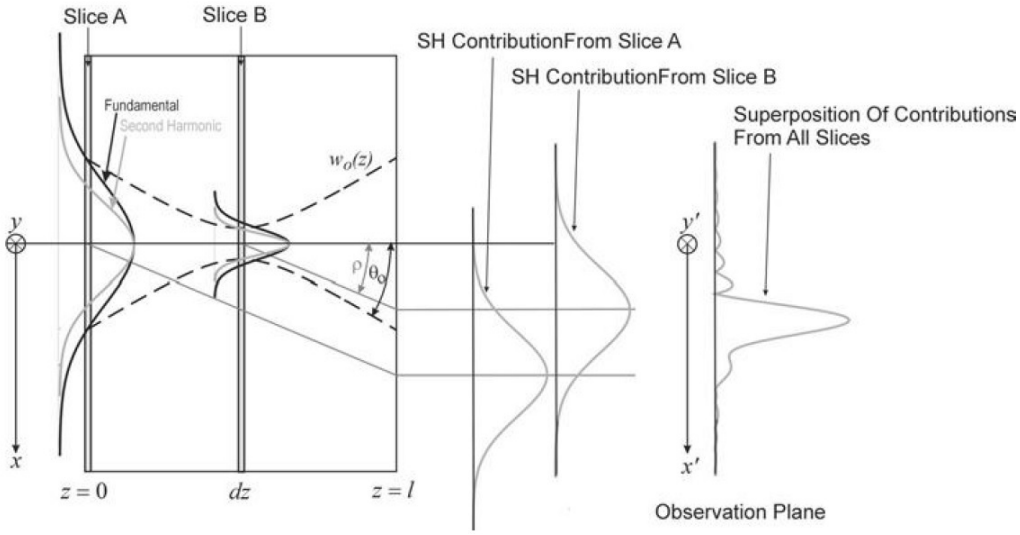

Figure 1.8: Scheme of SHG contribution from different crystal slices, leading to a distortion in the generated light profile (picture taken from [4]).

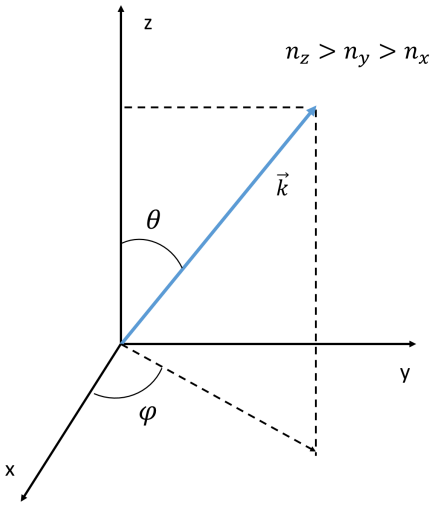

Figure 1.9: Axes frame for a biaxial crystal.

1.3 SHG conversion efficiency η

In the previous sections we briefly described the theory of SHG, and we outlined the importance of the phase matching condition. Here, we focus our attention on the efficiency of the frequency doubling process, in order to design our experimental set-up in the most convenient way; we follow the treatment given in [2] and [29].
First of all we recall Eq (1.21) for plane waves in the perfect phase matching condition $\Delta k = 0$:

$$I(\omega_2, l) \propto |I(\omega_1)|^2 l^2 \tag{1.33}$$

In writing it, we implicitly assumed to be in the low conversion efficiency regime, i.e, we took the input intensity $I(\omega_1)$ to be constant during the propagation through the nonlinear medium. When the conversion efficiency is high enough to significantly reduce the input intensity, the spatial variation through the nonlinear crystal of the fundamental and the generated fields is described by the following coupled equations:[3]

$$\begin{aligned} \frac{dE(\omega_1, z)}{dz} &= \frac{2i\omega_1^2 d_{eff}}{k_1 c^2} E(\omega_2, z) E^*(\omega_1, z) e^{-i\Delta k z} \\ \frac{dE(\omega_2, z)}{dz} &= \frac{i\omega_2^2 d_{eff}}{k_2 c^2} |E(\omega_1, z)|^2 e^{i\Delta k z} \end{aligned} \tag{1.34}$$

This system, together with the condition $I_{tot} = I(\omega_1) + I(\omega_2) = const$, can be solved with the definition of two adimensional real amplitudes $u_1(z)$, $u_2(z)$ [2], related to the fields by the relation:

$$E(\omega_i, z) = \left(\frac{I_{tot}}{2 n_i \epsilon_0 c} \right)^{1/2} u_i(z) e^{i\phi_i} \tag{1.35}$$

and satisfying the normalization condition:

$$u_1^2(z) + u_2^2(z) = 1 \tag{1.36}$$

An analytic solution for the perfect phase matching case is given by:

$$u_1(\zeta) = sech(\zeta) \tag{1.37}$$

$$u_2(\zeta) = tanh(\zeta) \tag{1.38}$$

[3] we are still in the Slow Varying Envelope approximation.

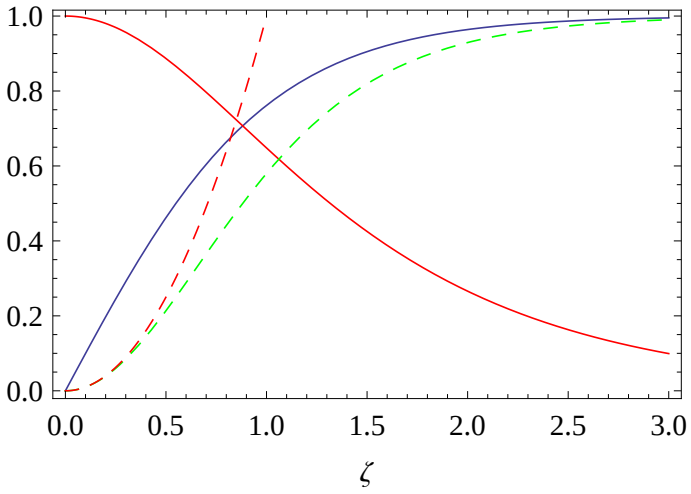

Figure 1.10: SHG conversion efficiency vs. crystal length in "characteristic length" units (Eq. (1.39)). Solid blue and red lines are u_1 and u_2 respectively. Green dashed line is the conversion efficiency η of Eq. (1.40); red dashed line is the efficiency in the low conversion efficiency regime (Eq(1.33)).

where $\zeta = z/l'$ and l' is a "characteristic length" defined as:

$$l' = \frac{c\sqrt{n(\omega_1)n(\omega_2)}}{2\omega_1 d_{eff}|E(\omega_1, 0)|} \tag{1.39}$$

In Figure 1.10 we report $u_1(\zeta)$, $u_2(\zeta)$ and the conversion efficiency defined as

$$\eta = \frac{u_2(z)^2}{u_1(0)^2} \tag{1.40}$$

We notice that in the low efficiency regime ($\eta < 10\%$) η grows quadratically (red dashed line) with z, as expected from equation (1.33); then, for long crystals, it approaches one, meaning that the input light is totally converted into the second harmonic beam.

From Eq. (1.33) and from the quadratic dependence of $I(\omega_2)$ on $I(\omega_1)$, it is apparent that the efficiency of the SHG can be increased significantly if tightly focussed, rather than collimated beams, are employed. In this case, what derived so far for plane waves must be modified, in order to correctly account for the spatial variation of the beams propagating through the crystal.

The formal treatment of SHG for Gaussian beams was made by Boyd and Kleinmann [29]. The basic idea is to divide the crystal into a sequence of infinitesimal slabs of thickness dz: the total second harmonic field outside the crystal is obtained by integrating the contribution of single slabs over the crystal length l, taking their relative phase into account. Without entering into the details of the calculation, we report here only the final expression for the generated power:

$$P_{2\omega} = K P_{\omega}^2 l k_1 e^{-\alpha l} h(\sigma, B, \kappa, \xi, \mu) \tag{1.41}$$

where

- $K = \frac{2\omega_1^2}{\pi c^3 \varepsilon_0 n^2(\omega_1) n(\omega_2)} d_{eff}^2$
- P_ω is the total incoming power
- k_1 is the fundamental wavevector inside the crystal
- $\alpha = \alpha(\omega_1) + \alpha(\omega_2)/2$ is the "total" absorption coefficient per length unit of the crystal

The function $h(\sigma, B, \kappa, \xi, \mu)$ is defined as:

$$h(\sigma, B, \kappa, \xi, \mu) = \frac{1}{4\xi} \iint_{-\xi(1-\mu)}^{\xi(1+\mu)} d\tau d\tau' \frac{e^{[i\sigma(\tau-\tau') - \frac{B^2}{\xi}(\tau-\tau')^2 - \kappa(\tau+\tau')]}}{(1+i\tau)(1-i\tau')} \tag{1.42}$$

with parameters:

$$\begin{aligned} \sigma &= \frac{1}{2} b \Delta k \\ B &= \frac{\rho\sqrt{l k_1}}{2} \\ \xi &= l/b \\ \mu &= (l-2f)/l \\ \kappa &= \frac{1}{2}\alpha b \end{aligned} \tag{1.43}$$

Finally, $b = 2z_0 = 2\pi\frac{w_0^2}{\lambda}$ where z_0 is the Rayleigh length of the fundamental beam, f is the coordinate of its focus with respect to the crystal input facet, and ρ is the walkoff angle (see Figure 1.11).

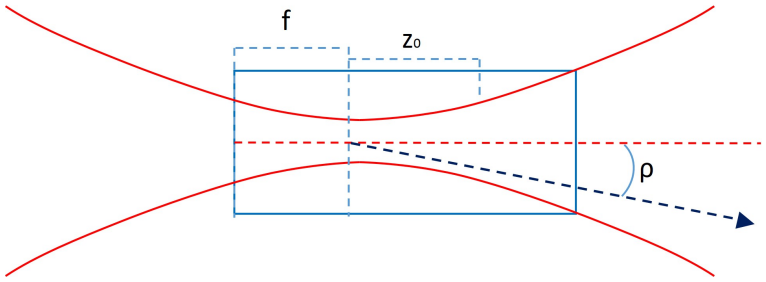

Figure 1.11: Scheme of fundamental and SHG beams inside the crystal. The blue dashed arrow indicates the propagation axis of the generated beam.

It is important to stress that the absorption coefficient α depends only on the crystal properties, while d_{eff}, ρ, $k_1, n(\omega_1), n(\omega_2)$ depend also on the direction in which fields propagate inside the medium. These quantities are then fixed once the phase matching condition is defined (sect. 1.2.1). The crystal length is taken here as a fixed parameter. On the other hand, σ, ξ, μ are all parameters that can be adjusted to maximize $h(\sigma, B, \kappa, \xi, \mu)$. In Figure 1.12 we report the original plot of the function $h_m(B, \xi) = h(\sigma_m, B, \xi, \kappa = \mu = 0)$ of the Boyd-Kleinmann paper, where σ_m is the optimum σ. μ, κ are taken equal to zero, i.e. the focus is assumed to be at half the crystal length, and absorption are neglected.

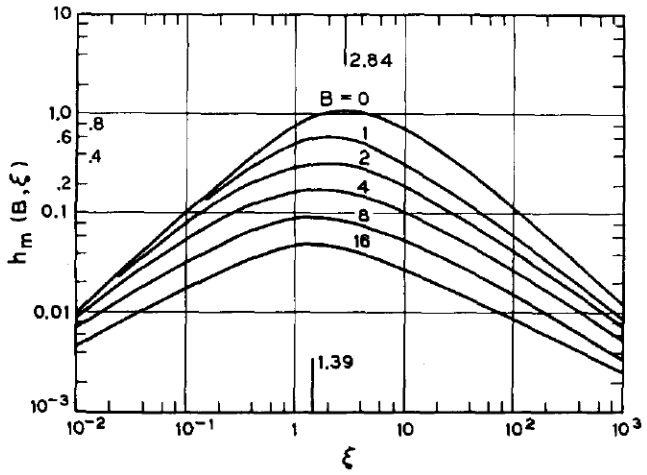

Figure 1.12: Boyd-Kleinmann function $h_m(B, \xi)$ for different B parameters. Picture taken from [29].

We can see from the figure that:

- $h_m(B, \xi)$ has always one single maximum.
- the maximum of $h_m(B, \xi)$, hence the maximum efficiency, decreases for increasing B, i.e. for greater walkoff angles.

It is worth also noticing that, based on the plane wave approximation described in the previous section, we would expect the optimum "mismatch parameter" σ to be equal to zero, corresponding to what we called "perfect phase matching". In contrast this reasoning is not perfectly accurate for the case of focused gaussian beams, which can be considered as containing plane waves having a range of propagation angles, i.e. having wave vectors "spread out" over a cone. Figure 1.13 shows $h(\sigma, \xi, B, \kappa = \mu = 0)$ as a function of σ for fixed ξ and for $\kappa = \mu = 0$: we can see that the maximum is reached for $\sigma > 0$, hence for $\Delta k > 0$ [4].

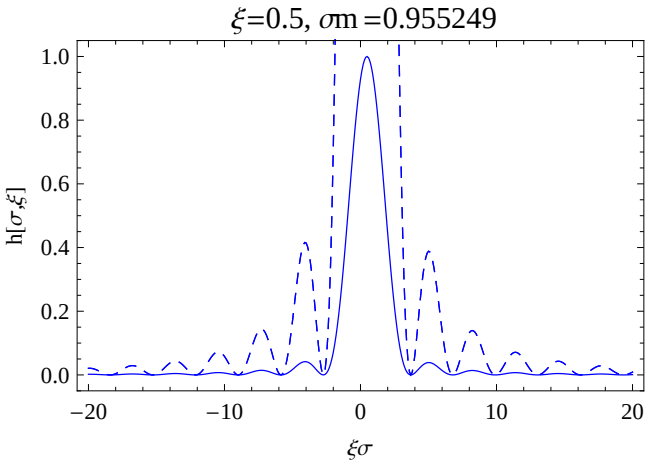

Figure 1.13: $h(\sigma, \xi)$ vs $\xi\sigma$; the dashed line is the function 10× enlarged.

[4] This mismatch is a small correction to $\Delta k = 0$, and corresponds to a $\Delta n = n(\omega_1) - n(\omega_2) \approx 10^{-5}$ to 10^{-6}; it will be achieved experimentally by tilting the crystal or by varying its temperature.

1.4 Crystals choice and evaluation of η

So far we described the theory concerning the SHG process, from a simplified plane wave approach to the realistic case of focused gaussian beam.
From what we have described, the best choice will be obviously to use a crystal with high nonlinear coefficient d_{eff}, small walkoff angle and small absorption coefficient. Actually, the choice of the crystal results as a compromise among these requests, and it also depends on other features as for example the power damage threshold of the crystal, the crystal quality and the available dimensions. In this work, where we want to obtain via SHG blue laser light at $425.5nm$, we focus our attention on 3 types of crystals: "BBO" (BaB_2O_4), "LBO" (LiB_3O_5) and "BIBO"(BiB_3O_6): BBO is an uniaxial crystal, while both LBO and BIBO are biaxial.
We developed a Mathematica code which allows us to evaluate all the quantities of interest described in previous sections (see Appendix 1). In particular, the first thing we find is the propagation and polarization angles to fulfill the phase matching condition, from which we find the nonlinear effective coefficient d_{eff} (Eq. (1.18)) with the formulas:

$$d_{effLBO} = d_{32}\cos\phi \tag{1.44}$$

$$d_{effBBO} = d_{31}\sin\theta - d_{22}\cos\theta \tag{1.45}$$

For the BIBO crystal the relation is rather more complicated and we took the value of d_{eff} using the $SNLO$ software (see Appendix A). Then we proceed for estimating the efficiency $\eta = P_{2\omega}/P_{\omega}$ of the SHG process for a given P_{ω} following these steps:

1. Set the crystal length
2. Calculate B given by Eq. (1.43)
3. Find the values of σ_{max} and ξ_{max} which maximize $h(\sigma, B, \kappa, \xi, \mu)$
4. Calculate η from Eq. (1.41)

The crystal length has to be optimized numerically in order to obtain the maximum SHG efficiency. This optimization process will be explained in section 2.6 (see Fig. 2.7). Here we can assume it is a fixed input parameter. In Table 1.1 we summarize the specifications of our chosen crystals for SHG at $\lambda_1 = 851nm$.

	BBO	LBO	BIBO
d_{eff} (pm/V)	2.01	0.78	3.60
ρ $(mrad)$	65.0	14.85	52.7
$\alpha(\omega_1)(\%cm^{-1})$	0.2	0.1	< 0.1
$\alpha(\omega_2)(\%cm^{-1})$	0.5	0.5	< 0.1
$n(\omega_1) = n(\omega_2)$	1.66	1.61	1.85
θ	27.5^o	90^o	155.3^o
φ	$---$	27^o	90^o

Table 1.1: Specifications of BBO, LBO, BIBO for SHG at $\lambda_1 = 851nm$. The values are obtained both from our simulations and from a survey of different numbers coming from manufacturers and papers [33].

LBO and BBO are commonly used crystals for SHG in the blue range; BIBO is a more recently developed crystal, with very high d_{eff}, and therefore potentially very interesting. However, a few recents papers [43, 44] report about some instabilities in the SHG process for high values of incident power.
We can calculate now all the quantities of interest for our crystals; we report them in Table 1.2 for $1.5W$ of incident power, a value close to the maximum we can achieve amplifying our master laser (see chapter 3).
In Figure 1.14 we plot the single-pass efficiencies as a function of ξ.
Here one can see that the maximum efficiencies are very low, of the order of $10^{-4} - 10^{-5}$. This is the reason why we will need the other fundamental element of our work: the frequency doubling cavity, which will ensure high incident powers on the crystal, ~ 100 times the input power value (see sect. 2.4). Since the SHG beam power grows quadratically with the fundamental beam power (Eq. (1.41)), the cavity will allow us to increase the overall

efficiency by a factor $10^3 - 10^4$.

	BBO	LBO	BIBO
Length (mm)	12	15	10
B	12.5	3.1	9.7
ξ_m	1.43	1.55	1.45
σ_m	0.75	0.75	0.74
h_m	0.05	0.2	0.07
$w_0(\mu m)$	26.1	28.5	22.7
$z_0(mm)$	4.2	4.8	3.4
η	$9.6 * 10^{-5}$	$7.2 * 10^{-5}$	$2.7 * 10^{-4}$

Table 1.2: Optimized parameters for BBO, LBO and BIBO crystals for 1.5W incident power, obtained with our Mathematica code.

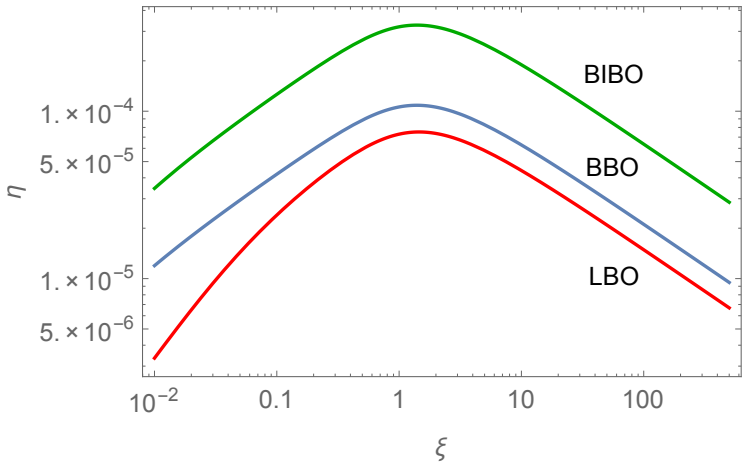

Figure 1.14: Calculated efficiencies for BBO (blue; B=16), LBO (red; B=3.6), BIBO (green; B=13.8) as a function of ξ for 1.5W input power.

Chapter 2

Frequency Doubling Cavity

The cavity is a fundamental element for increasing the efficiency of the SHG process, providing a power on the crystal up to ~ 100 times the laser power at the cavity input. We choose to build a "bow-tie" ring cavity: it is a travelling wave cavity, that provides a full spatial exploiting of the crystal (in contrast to what happens with linear standing wave cavities). In this chapter we describe first the cavity design, then we present the calculation for the power enhancement factor and for the cavity spectrum.

2.1 Cavity Design

The cavity design we have chosen is sketched in Figure 2.1. It is a symmetric bow-tie cavity composed of two planar mirrors (M1, M2) and two spherical mirrors (M3, M4) with radius of curvature of $100mm$. The light is coupled into the cavity at M1, and the crystal is placed between the spherical mirrors. As we will see later, the waist inside the crystal sensitively depends on the relative distance between M4 and M3, and therefore it can be easily adjusted. M4 is a dichroic mirror, with high reflectivity in the infrared region and high transmittivity in the visible; this allows the blue light to leave the cavity after it is generated inside the crystal. Therefore, M4 represents the output of the cavity for the 425.5nm radiation.
As shown in the figure, the blue light is generated only in one direction, in

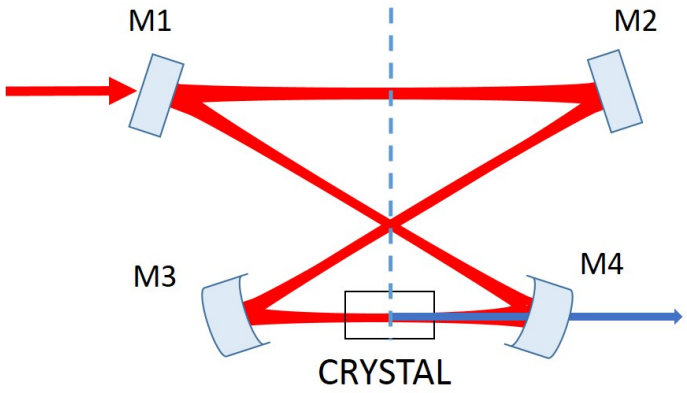

Figure 2.1: Bow-tie cavity scheme; dashed line is the cavity symmetry axis. The incoupling mirror M1 reflectivity is chosen to match the losses and conversion efficiency (Eq. (2.30)), and the other mirrors have high reflectivity ($> 99.9\%$) at 850nm and low reflectivity ($< 5\%$) for the 425nm light. For details see chapter 4.

contrast to what happens in linear cavities where light is emitted from both sides of the crystal.

In general, the properties of a gaussian beam at a particular point z along its axis can be encoded in the complex beam parameter $q(z)$ [1]. This can be calculated from the beam's wavelength λ_0, the radius of curvature $R(z)$ of the wavefront, and the beam waist $w(z)$ according to:

$$\frac{1}{q(z)} = \frac{1}{R(z)} - i\frac{\lambda}{\pi w^2(z)} \tag{2.1}$$

We summarize below the expression of the principal beam parameters, which will be useful in the following.

$$\begin{aligned} z_0 &= \frac{\pi w_0^2}{\lambda} \\ w(z) &= w_0\sqrt{1+\left(\frac{z}{z_0}\right)^2} \\ R(z) &= z\left[1+\left(\frac{z_0}{z}\right)^2\right] \end{aligned} \tag{2.2}$$

where z_0 is known as the Rayleigh length.

The propagation of a Gaussian beam in the presence of optical elements

is described by the well known $ABCD$ law, which is based on ray transfer matrices. A Gaussian beam, after passing through an optical element, will change its properties in agreement with:

$$q_2 = \frac{Aq_1 + B}{Cq_1 + D} \tag{2.3}$$

Here q_1 and q_2 are the complex beam parameter in front of and behind the optical element respectively. $M = \begin{bmatrix} A & B \\ C & D \end{bmatrix}$ is the ray transfer matrix of the optical element, defined from the relation:

$$\begin{pmatrix} y_2 \\ y_2' \end{pmatrix} = \begin{bmatrix} A & B \\ C & D \end{bmatrix} \begin{pmatrix} y_1 \\ y_1' \end{pmatrix} \tag{2.4}$$

where y is the coordinate of the point of incidence of the ray on the element, taken with respect to the element optical axis, and y' is the tangent of the angle between the ray and the optical axis[1]. The indexes 1 and 2 are respectively for incident and exiting rays. When we apply ray matrices to Gaussian beams, the beam axis plays the role of the ray direction.
The important point of the transfer matrices formalism is that the propagation of a beam through a succession of optical elements can be described via Eq. (2.4) using a matrix that is the product of single transfer matrices. The round trip of our cavity can then be described with a single, easy-to-calculate matrix; the properties of the beam propagating inside the cavity will come out directly using the ABCD law with the "total" round trip matrix.
A stable solution for the beam inside the cavity will in fact remain unchanged after a round trip; i.e. it will satisfy the condition:

$$q_2 = \frac{Aq_1 + B}{Cq_1 + D} = q_1 \tag{2.5}$$

where A, B, C, D are the elements of the round trip matrix.

[1]In the paraxial approximation we approximate y' directly with the angle. Sometimes a different convention is used, where the slopes are multiplied by the refractive index. The matrices in Table 1 change accordingly.

optical element	ray matrix		
free space	$M_{space}(L)$	$=$	$\begin{bmatrix} 1 & L \\ 0 & 1 \end{bmatrix}$
thin lens	$M_{lens}(f)$	$=$	$\begin{bmatrix} 1 & 0 \\ -\frac{1}{f} & 1 \end{bmatrix}$
planar mirror	M_{pm}	$=$	$\begin{bmatrix} 1 & 0 \\ 0 & 1 \end{bmatrix}$
planar boundary	$M_{pb}(n_1, n_2)$	$=$	$\begin{bmatrix} 1 & 0 \\ 0 & \frac{n_1}{n_2} \end{bmatrix}$
spherical mirror	$M_{sm}(r)$	$=$	$\begin{bmatrix} 1 & 0 \\ \frac{2}{r} & 1 \end{bmatrix}$
spherical boundary	$M_{sb}(r, n_1, n_2)$	$=$	$\begin{bmatrix} 1 & 0 \\ -\frac{n_2 - n_1}{n_2\, r} & \frac{n_1}{n_2} \end{bmatrix}$

Table 2.1: Transfer matrices for the principal optical elements.

To calculate our round trip matrix we need then to know the transfer matrices of free space, planar mirrors, curved mirrors and planar boundaries (for the crystal/air passage). These matrices can be evaluated from the definition (2.3) and we report them in the Table 2.1.
We show now as an example how to calculate the matrix corresponding to half a cavity round trip, taking the starting point in the center of the crystal. With reference to Figure 2.2, we divide the propagation in five steps:

1. Propagation inside the crystal for $l/2$
2. Crossing of crystal/air interface
3. Free space propagation for $(Z - l)/2$
4. Reflection from spherical mirror M4
5. Free space propagation for $(L - Z)/2$

In step 5 we took into account that the reflection from the planar mirror M1 corresponds to the identity matrix (see Table 2.1).

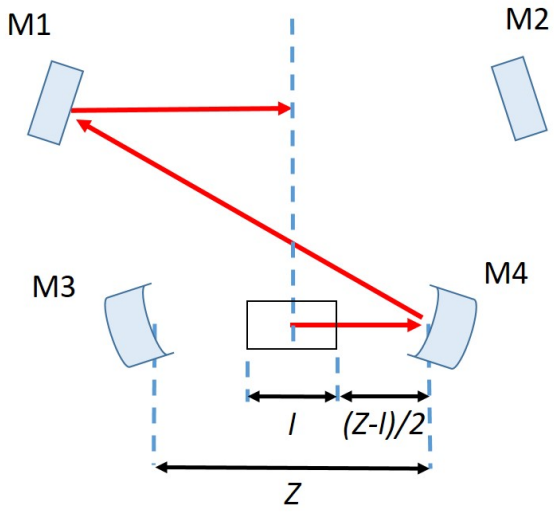

Figure 2.2: Half-cavity propagation scheme; round trip distance=L.

The half-round trip ray matrix is then calculated as:

$$M_{half\ trip} = M_5 \cdot M_4 \cdot M_3 \cdot M_2 \cdot M_1 =$$
$$= \begin{bmatrix} 1 & (L-Z)/2 \\ 0 & 1 \end{bmatrix} \cdot \begin{bmatrix} 1 & 0 \\ \frac{2}{r} & 1 \end{bmatrix} \cdot \begin{bmatrix} 1 & (Z-l)/2 \\ 0 & 1 \end{bmatrix} \cdot \begin{bmatrix} 1 & 0 \\ 0 & n \end{bmatrix} \cdot \begin{bmatrix} 1 & l/2 \\ 0 & 1 \end{bmatrix} \tag{2.6}$$

where n is the refractive index of the crystal (we take $n_{air} = 1$). We find in an analogous way the total round trip matrix. We calculate two different versions of the round trip matrix: one taking $z = 0$ in the center of spherical mirrors arm, the other one taking $z = 0$ in the center of the planar mirrors arm. This is for the reason that we expect the cavity beam to have two foci in those positions. Requiring the condition (2.5) to be satisfied for any of these matrices we can calculate all the parameters of the cavity beam.

2.2 Cavity Spectrum

In this section we explain how we calculate the cavity spectrum. It can be shown [1] that a complete orthonormal basis for describing the intensity

profile of an arbitrary propagating beam is given by the so-called *Gauss-Hermite Modes* TEM_{mq} defined as:

$$TEM_{mq} \propto H_m\left(\frac{\sqrt{2}}{w(z)}x\right) H_q\left(\frac{\sqrt{2}}{w(z)}y\right) e^{-\frac{x^2+y^2}{w(z)^2}} \tag{2.7}$$

Where H_m are the Hermite polynomials:

$$H_m(x) = (-1)^m e^{x^2} \frac{d^m}{dx^m} e^{-x^2} \tag{2.8}$$

For our purposes we want to couple all the input power to the so-called longitudinal TEM_{00} cavity mode which has a pure Gaussian profile and the smallest size among all possible modes. If some of the power is coupled to higher-order (so-called transverse) modes the SHG efficiency is reduced. The power of these modes is in fact distributed in a spatial pattern of light and dark zones (see fig. 4.3): the SHG process for transverse modes happens then in different crystal regions, leading to a reduced intensity and conversion efficiency (see Eq. (1.41)) and to a strongly distorted profile of the blue beam. A Gauss-Hermite mode propagating in a medium for a distance z accumulates a phase along its propagation axes given by [1, 2]:

$$\phi(z) = kz + k\frac{x^2+y^2}{2R(z)} - (m+q+1)\zeta(z) \tag{2.9}$$

The term

$$\zeta(z) = arctan\left(\frac{z}{z_0}\right) \tag{2.10}$$

is known as the "Gouy phase" and it can be seen as the phase difference of a Gaussian beam with respect to a plane wave. The resonant modes of the cavity, hence the cavity spectrum, are set by the condition:

$$\phi_{trip} = 2\pi p \qquad p \text{ integer} \tag{2.11}$$

i.e. imposing that their round trip reflections interfere constructively. The term kz in Eq. (2.9) corresponds to the phase of a plane wave. To calculate this term for our cavity round trip we have to consider both the propagation

inside the crystal (of refractive index n) for a length l, and in the air ($n_{air} = 1$) for a length $L - l$. We can easily get:

$$\phi_{trip} = \frac{2\pi\nu}{c}(L + l(n-1)) - (m + q + 1)\zeta(L) \tag{2.12}$$

For the round trip Gouy phase $\zeta(L)$ we have to remember the presence of two foci inside the cavity with different Rayleigh lengths z_0 (see Sect. 2.1). Because z_0 enters in the definition (2.10), we have to think our beam as composed of two beams with different Rayleigh lengths meeting at the curved mirrors edges with the same wavefront; we calculate the phase separately for these fictitious beams and we sum them to find $\zeta(L)$.
Let us then consider for simplicity half a round trip like in Figure 2.2 and let us split the beam in two: one first beam with focus inside the center of the crystal, waist w_{01}, propagating for a distance $Z/2$; the other with the focus in the center of the planar mirrors arm, waist w_{02}, propagating for a distance $(L - Z)/2$. The Gouy phase of half a round trip is the sum of these contributions:

$$\zeta(L/2) = arctan\left[\frac{Z}{2z_{01}}\right] + arctan\left[\frac{L-Z}{2z_{02}}\right] \tag{2.13}$$

We obtain then for the total round trip phase:

$$\phi_{trip} = \frac{2\pi\nu}{c}(L + l(n-1)) - 2(m + q + 1)\zeta(L/2) \tag{2.14}$$

where we have used for the total Gouy phase $\zeta(L) = 2\zeta(L/2)$.
With this relation we are now able to calculate the cavity spectrum. From the condition (2.11) we find the resonance frequencies of the cavity to be:

$$\nu_{pmq} = \frac{c}{L + l(n-1)}\left(p + (m + q + 1)\frac{\zeta(L)}{\pi}\right) \tag{2.15}$$

from which we can see that transverse modes with same $m + q$ value are degenerate in frequency. The free spectral range (FSR), defined as the distance between two successive longitudinal modes, is simply calculated as:

$$FSR = \frac{c}{L + l(n-1)} \tag{2.16}$$

The frequency spacing $\Delta\nu_T$ between two adjacent transverse modes is calculated from equation (2.15) taking the same p and setting $m_2+q_2 = m_1+q_1+1$; in this way we find:

$$\Delta\nu_T = FSR\frac{\zeta(L)}{\pi} \tag{2.17}$$

We conclude this section reminding that what written so far holds for ideal cavities. For a real cavity, inhomogeneities in the beam propagation along the horizontal and the vertical axes can lead to different effective optical lengths, thus to slightly different resonant frequencies for transverse modes of the same order (see Sect. 5.1.1).

2.3 Finesse

Another important parameter for the cavity characterization is the finesse $\mathcal{F}$, defined as the ratio between the free spectral range and the TEM_{00} mode linewidth:

$$\mathcal{F} = \frac{FSR}{\Delta\nu} \tag{2.18}$$

This parameter depends only on the cavity losses, which are given in our case by the mirror reflectivities, the crystal losses and the SHG process. n expression for $\Delta\nu$ can be found with an analysis of the interference of multiple reflected beams inside the cavity [4].

Let us first consider the simple case of a linear cavity: with reference to Figure 2.3, it is straightforward to obtain for the internal field:

$$E_{cav} = E_{in}t_1\sum_{n=0}^{\infty}(r_1r_2e^{2ikd})^n = E_{in}\frac{t_1}{1-r_1r_2e^{2ikd}} \tag{2.19}$$

where r_i, t_i are the mirrors amplitude reflection and transmission coefficients. Evaluating the square modulus of eq. (2.19) the following relation for the power inside the cavity is obtained:

$$P_{cav} = P_{in}\frac{T_1}{(1-\sqrt{R_1R_2})^2 + 4\sqrt{R_1R_2}sin^2(\frac{\phi}{2})} \tag{2.20}$$

where $R_i = |r_i|^2, T_i = |t_i|^2$, and $\phi = 2kd$ is the round trip phase.

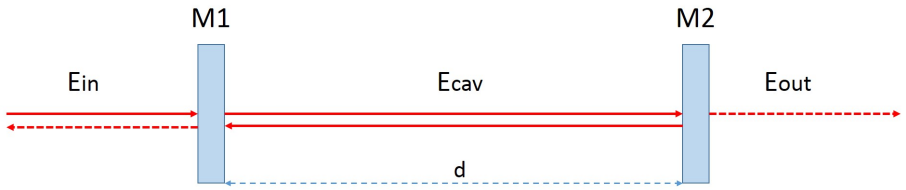

Figure 2.3: Linear cavity scheme. The multiple reflections from the mirrors interfere each others, leading to Eq. 2.19

.

The linewidth of the cavity mode is obtained by the phase difference $\Delta\phi_{FWHM}$ corresponding to the $FWHM$ (full-width-half-maximum) of the Lorentzian curve described by Eq. (2.20):

$$\Delta\phi_{FWHM} = 4arcsin\left(\frac{1-\sqrt{R_1R_2}}{2(R_1R_2)^{1/4}}\right) \tag{2.21}$$

Since for a given cavity length the phase difference is directly related to a frequency difference as:

$$\Delta\phi = 2\Delta kd = 4\pi\frac{\Delta\nu}{c}d = 2\pi\frac{\Delta\nu}{FSR} \tag{2.22}$$

By inserting Eq. (2.21) into Eq. (2.22), and given the definition (2.18) we find:

$$\mathcal{F} = \frac{\pi}{2arcsin\left(\frac{1-\sqrt{R_1R_2}}{2(R_1R_2)^{1/4}}\right)} \sim \frac{\pi(R_1R_2)^{1/4}}{1-\sqrt{R_1R_2}} \tag{2.23}$$

where we approximate $\arcsin\alpha \sim \alpha$, which is fully valid since we are considering high reflectivity mirrors ($R_i \geq 0.98$).
The expression for the bow-tie cavity can be found with the same calculations, with the only difference that we have to consider the presence of 4 mirrors. We have for this case:

$$\mathcal{F} \sim \frac{\pi(R_T)^{1/4}}{1-\sqrt{R_T}} \tag{2.24}$$

where $R_T = \prod_{i=1}^{4} R_i$. From Eq. (2.24) and from the definition (2.18) we straightforwardly obtain the linewidth:

$$\Delta\nu = FSR\frac{1-\sqrt{R_T}}{\pi(R_T)^{1/4}} \tag{2.25}$$

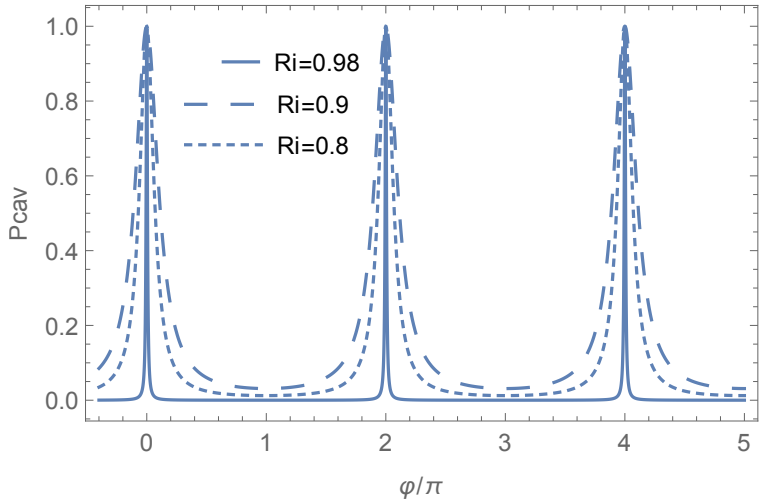

Figure 2.4: Normalized cavity power P_{cav} of eq. (2.20) for different values of mirrors reflectivities. We can see the ratio between the FSR and the linewidth of the peaks (i.e. the Finesse) is getting smaller for lower reflectivities.

When we consider the cavity with the SHG crystal in it, the finesse is reduced both for the losses V_c due to crystal absorption and reflection, and for the losses η due to the SHG (single pass) process. The equation for the power of the fundamental beam inside the cavity becomes then

$$P_{cav} = P_{in}\frac{T_1}{(1-\sqrt{R_T(1-V_c)(1-\eta)})^2 + 4\sqrt{R_T(1-V_c)(1-\eta)}sin^2(\frac{\phi}{2})} \tag{2.26}$$

which is the same of Eq. (2.20), replacing $R_T \to R_T(1-V_c)(1-\eta)$. By following the procedure described above, we find for this case a finesse $\mathcal{F}'$ and a linewidht $\Delta\nu'$:

$$\mathcal{F}' \sim \frac{\pi(R_T(1-V_c)(1-\eta))^{1/4}}{1-\sqrt{R_T(1-V_c)(1-\eta)}} \tag{2.27}$$

$$\Delta\nu' = FSR\frac{1-\sqrt{R_T(1-V_c)(1-\eta)}}{\pi(R_T(1-V_c)(1-\eta))^{1/4}} \tag{2.28}$$

Solving Eq. (2.27) or Eq. (2.28) with respect to η is possible to estimate the single pass SHG efficiency.

2.4 Power Enhancement

The cavity allows to store high optical power, which is fundamental to obtain a significant increase in the SHG conversion efficiency. When performing the calculations of the power inside the cavity, we have to consider the fact that the cavity power is affected by losses, that losses depend on the SHG (single pass) conversion efficiency, and that the efficiency depends on the power incident on the crystal. We need then an iterative process to find the steady amount of power within the cavity.
Ref. [30] provides a numerical analysis of the problem based on the Boyd-Kleinmann theory (sect. 1.3). This analysis starts assuming a value of the resonant enhancement factor $\epsilon = \frac{Pcav}{P_{in}}$ of the ring cavity given by Eq. (2.26), evaluated at resonance ($\phi = 0$):

$$\epsilon = \frac{1 - R_1}{(1 - \sqrt{(1 - V_c)(1 - \eta)R_1 R_{HR}^3})^2} \tag{2.29}$$

where we take M2, M3, M4 (Fig. 2.1) to be equal high reflectivity mirrors ($R_{HR} > 0.99$). Maximizing Eq. (2.29) with respect to R_1 we obtain the optimum input mirror reflectivity and cavity enhancement:

$$\begin{aligned} R_1^{opt} &= (1 - V_c)(1 - \eta)R_{HR}^3 \\ \epsilon_{opt} &= \frac{1}{1 - R_1^{opt}} \end{aligned} \tag{2.30}$$

We choose then R_1 in accordance with this value, using for η the value found with the iterative process we describe in the Section 2.6.

2.5 Cavity Stability

We report now some consideration about the cavity stability. Equation (2.15) is often written as:

$$\nu_{qmn} = FSR\left(p + (m + q + 1)\frac{cos^{-1}(\pm\sqrt{g_1 g_2})}{\pi}\right) \tag{2.31}$$

where

$$g_1 = 1 - \frac{L - Z}{r}, \quad g_2 = 1 - \frac{Z}{r} \tag{2.32}$$

and r is the radius of curvature of the spherical mirrors. These parameters are important to understand whether our cavity is stable. From the ABCD law, which gives imaginary waists outside the stable region, one can define a stability criterion [1]:

$$0 \leq g_1 g_2 \leq 1 \tag{2.33}$$

When this condition is not satisfied the cavity does not produce periodic refocussing of the intracavity beam, i.e. there are no stable solutions.

2.6 Our cavity

We report now the experimentally relevant parameters calculated on the basis of what explained in the previous sections.

Cavity Design

We see from Table 1.2 of section 1.4 that the waists we want to have inside the different kinds of crystal range between $\sim 23\mu m$ and $\sim 29\mu m$. With a Mathematica code (see Appendix A) we can easily modify the cavity parameters in order to control the beam waist inside the crystal. Using mirrors with 100 mm radius of curvature we can obtain the optimal waists for example by setting $L - Z = 450$ mm and $Z = 107$ to 109 mm. These are indicative values useful to start setting up the cavity; what we will experimentally do is to adjust the different parameters like mirrors relative distances, crystal angle etc. in order to find the maximum output power in the most stable configuration.

Cavity Spectrum

In Figure 2.5 we report an example of the calculated spectrum of our cavity with the LBO crystal for $L = 557mm$ and $Z = 107mm$, on the basis of what we discussed above.
The red line is the TEM_{00} mode, i.e. the frequency $\nu_{1,0,0}$; next we see the higher order transverse modes. The transverse mode nearest to the TEM_{00}

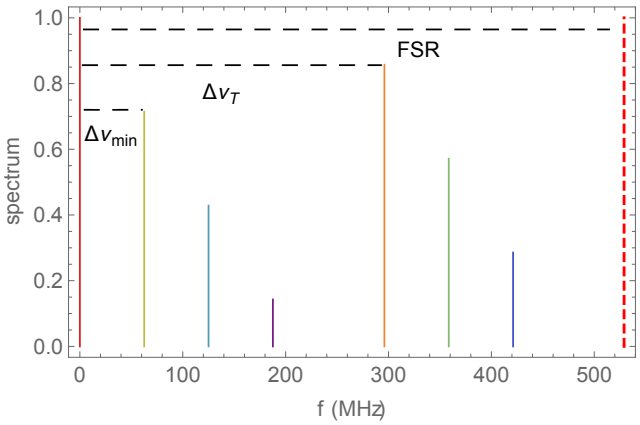

Figure 2.5: Calculated cavity spectrum for the LBO crystal. Only the central wavelengths of the first 7 modes are plotted. The increasing modes are ordered in decreasing height, i.e. the red highest mode is the TEM_{00}, the orange is the TEM_{10}/TEM_{01} and so on. The red dashed line indicates the FSR; we can see transverse modes belonging to different longitudinal modes overlapping.

is a third order mode ($m + n = 3$) overlapping from a different longitudinal mode; the distance between them is $\Delta\nu_{min} \sim 62MHz$, and the Free Spectral Range is $\simeq 529MHz$. We find similar values for the other crystals. At the beginning of section 2.5 we said we wanted to avoid the coupling of the input light with other modes than the longitudinal TEM_{00} mode. This requirement is satisfied if:

1. the linewidth $\Delta\nu_{master}$ of the master laser light injecting the cavity is narrower than $\Delta\nu_{min}$

2. the linewidth $\Delta\nu$ of the cavity modes is narrower than $\Delta\nu_{min}$

The first point in surely satisfied, since we will use a laser with a $\Delta\nu_{master} < 1MHz$. The second point is also satisfied, because we estimate a mode linewidth of $\simeq 2MHz$ (Eq. (2.28)). We know actually that we have to keep free a wider spectral zone, of $\simeq 12.5MHz$, for the cavity locking (see chapter 4), but this does not represent a problem since we have $\Delta\phi_{min} > 12.5MHz$.

Power Enhancement and Optimal Crystal Length

The power enhancement factor is calculated with an iterative process using a Mathematica program (Appendix A) that works as follows: first it calculates the waist of the beam inside the crystal for a given crystal length, corresponding to the optimum focusing parameter ξ; then we give as fixed input parameters the cavity input power P_{in}, V_c and mirrors reflectivities. The program finds the cavity power for an initial ϵ_0 that we reasonably estimate a priori as order of magnitude. Then the program calculates from Eq. (2.29) the losses corresponding to ϵ_0 and recalculates ϵ. The process goes on until it converges. We underline that the cavity power will not grow linearly with P_{in}: the power enhancement factor ϵ is in fact not a constant value. The cavity losses due to the term η will grow for higher powers, reducing the power enhancement (Figure 2.6). Both these effects are stronger for higher cavity finesses.

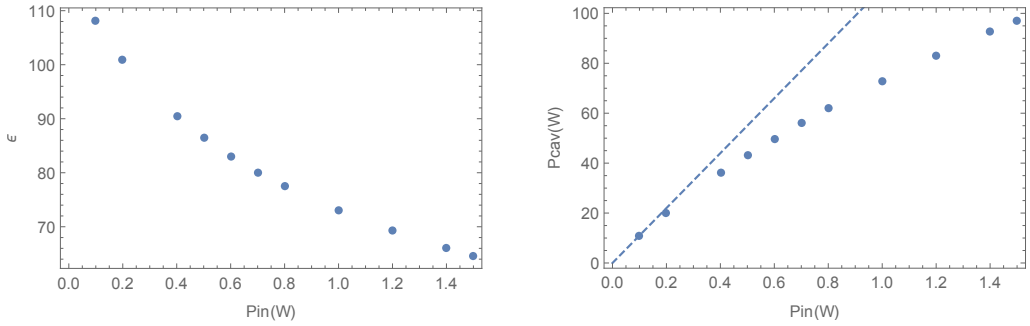

(a) Cavity power enhancement ϵ vs. P_{in}.

(b) Cavity power P_{cav} vs. P_{in}.

Figure 2.6: Calculated values for the ϵ and P_{cav}.

With our code we obtain for the LBO crystal an enhancement factor $\epsilon = 74$ for $R_{HR} = 0.9993$, $R_{M1} = 0.98$ and $P_{in} = 1W$, a value close to the maximum power we will inject into the cavity. The incident power on the crystal is then $P_{cav} = \epsilon P_{in} = 74W$, leading to $\approx 423mW$ of blue light ($\eta = 0.005$). The "total" efficiency of the SHG process within the cavity, given by

$$\eta_{tot} = P_{blue}/P_{in} = \epsilon * \eta \tag{2.34}$$

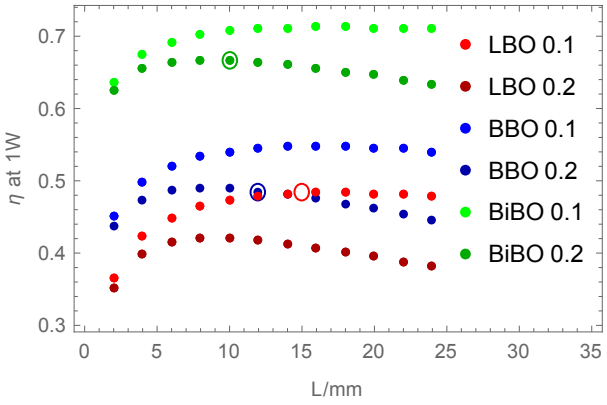

Figure 2.7: Total efficiency as a function of crystal lengths for BBO, BIBO, LBO, for different values of the total absorption coefficient (0.1, 0.2). Circles show our chosen lenght.

is in this case $\sim 42\%$. For BBO we find similar values, while for BIBO we have $\eta_{tot} \sim 61\%$. If we compare this value with the single pass process efficiency given in section 1.4 we can see an increase by a factor 10^3.

The other important parameter we can optimize with this program is the crystal length l. Varying the crystal length leads both to a variation in the absorption V_c and in η; we can find then the optimal crystal length as the one maximizing η_{tot} (see Figure 2.7). We can see all the maxima are for l between 10 and 15mm; we choose then to use a length of 15mm for the LBO, 12mm for the BBO and 10mm for BIBO.

Cavity Stability

Our cavity works at the edge of the stability region; with our values for L and Z we find $g_1 g_2 = 0.24$. In Figure 2.8 (a) we can see then what happens in the cavity spectrum when we change Z by a few millimeters: the modes get closer to each other for negative values of dz, until odd and even modes become degenerate and spaced of $FSR/2$ for a value $Z \sim 104.8mm$. This is the so-called "confocal configuration"; below this value the cavity is not stable anymore.
When getting too close to the confocal configuration we will reach a point

where some power starts to couple with transverse modes, i.e. the condition $\Delta\nu, \Delta\nu_{master} < \Delta\phi_{min}$ doesn't hold anymore. In figure 2.8 (b) we can see how the cavity spectrum is modified varying the total cavity length maintaining $Z = 107mm$: we can see the spectrum is much less sensitive to this variation. Varying Z has another important effect, shown in figure 2.8 (c), that is a significant variation of the waist inside the crystal: this is a relevant point since the conversion efficiency has a strong dependence on the focusing parameter ξ, as discussed in sect. 1.3. In our cavity design we have then to take into account this critical role of Z.

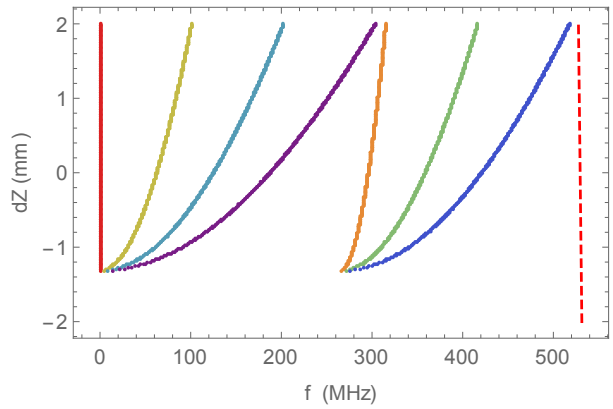

(a)

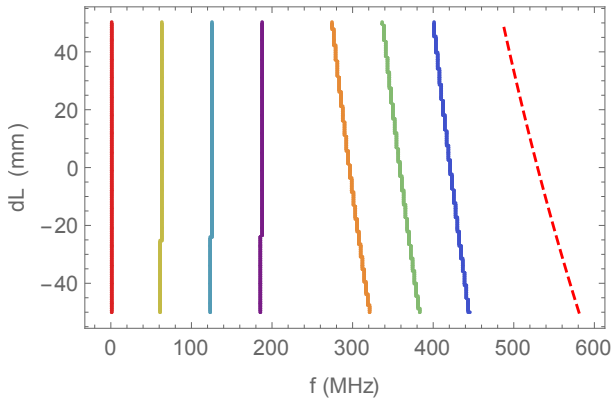

(b)

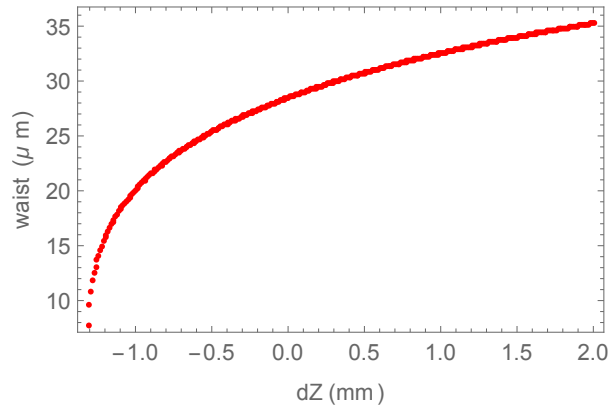

(c)

Figure 2.8: Cavity spectrum for variations of (a) Z and (b) L with respect to $Z = 107mm$ and $L = 557mm$ (b). The intersection of a horizontal line at a given value dZ or dL with the colored curves gives the frequency of higher order modes; the red dashed line indicates the FSR. (c): waist inside the crystal for a variation of Z with respect to $Z = 107mm$.

Chapter 3

Infrared Light

In this chapter we explain how we produce and manipulate the infrared light at $\lambda = 851nm$ that we inject into the frequency doubling cavity. The process can be divided in two steps: first, the power amplification of our master laser light, then the coupling into an optical fiber, whose output will be injected into the cavity.

3.1 Experimental Setup

In Figure 3.1 we represent the experimental setup of the light source and frequency doubling cavity. The 851nm laser source is a DL Pro from Toptica; it is an extended-cavity laser diode with tunable wavelength, and maximum output power of 170mW. For our purposes, we need to increase the infrared power to $\approx 3W$ in order to obtain 500 to $800mW$ of blue power. In fact, we expect a coupling efficiency of $\sim 60\%$ for the infrared light into the fiber (see section 3.1.2), and a conversion efficiency of about 45% (see section 2.4). In order to obtain such a high power we use a Tapered Amplifier.

3.1.1 The Tapered Amplifier

As suggested by the name, a Tapered Amplifier (TA in the following) is a semiconductor device which has a (lateral) tapered gain region. This device can in principle work both as an amplifier or as a laser, depending upon how

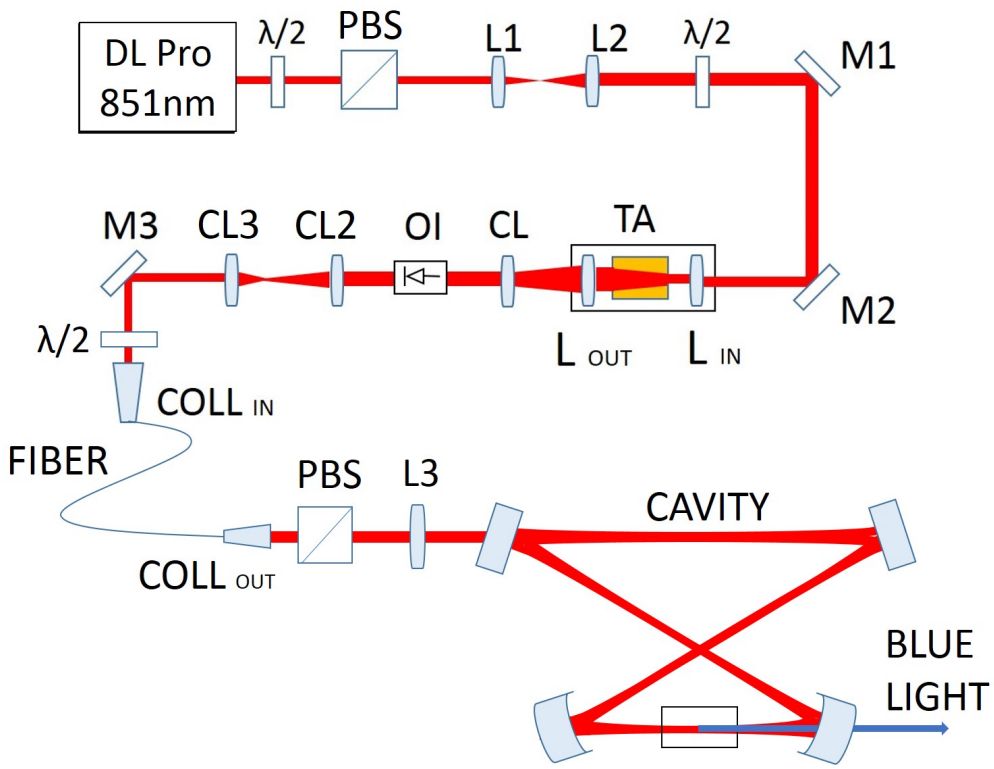

Figure 3.1: Scheme of the infrared light setup. Before the input collimator $COLL_{IN}$ there is the part designed for the amplification of the master laser light. The light outgoing from $COLL_{OUT}$ is coupled into the cavity described in sect. 2.1. PBS: Polarizing Beam Splitter; TA: Tapered Amplifier; OI: Optical Isolator. The cavity set up is described in details in chapter 4.

the input and output facets are coated, to provide either small or large facet reflectivities. Population inversion in the TA medium is achieved through electrical pumping. In order to obtain a uniform pumping the thickness of the chip has to be constant over the length of the TA.
The design of the TA consists of two sections monolithically integrated on one chip: an index-guided ridge-waveguide, and a gain-guided broad pumped area, designed to obtain high output power. As light propagates from the narrow end of the taper to the large end, the input beam expands laterally, owing to diffraction, and thereby fills the expanding cross-section of the device. If we consider e.g. a Gaussian beam at the input facet, it is easy to see that as the beam propagates it becomes more and more uniform in lat-

eral profile and eventually approaches the top-hat distribution. This occurs because the gain along the central axis of the tapered region saturates first because of the larger initial intensity in the centre of the beam. Hence, the edges experience higher gain until the whole wavefront saturates to a nearly uniform intensity. Of course, current spreading at the outer edges of the taper, diffusion of the carriers, non-linear effects in the gain medium, thermal effects and non-uniform current injection make the real beam description much more complicated, as we will see later.

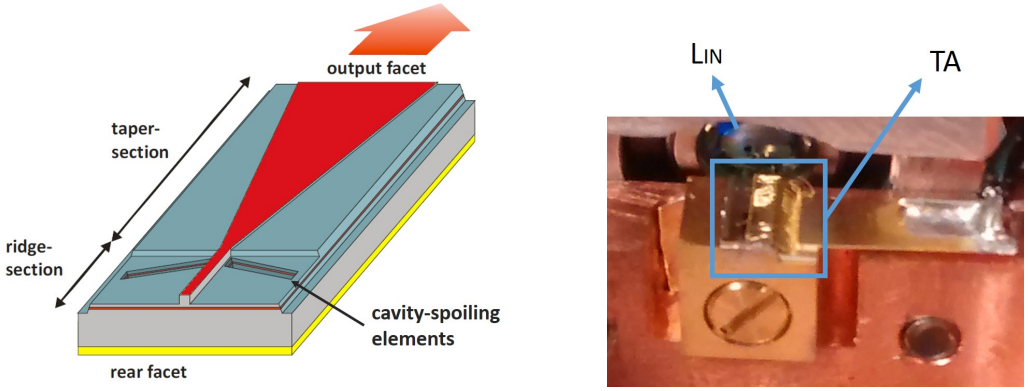

(a) (b)

Figure 3.2: (a): schematic representation of the TA. (b): real image of the TA chip m2k TA-0850-3000.

The TA we use is the GaAs-based device TA-0850-3000 from m2k Laser; the length of the tapered region is 4.3 mm; the output aperture is $256\mu m$ wide and the input aperture width is $\approx 3\mu m$; the full angle of the taper is 6^o.
In figure 3.2(a) we can see the cavity-spoiling elements, consisting of grooves etched down through the active region in the ridge-section, and angled with respect to the axis of the tapered structure to deflect and scatter undesired modes with wavefronts parallel to the two facets.
The thermal stabilization of the TA is a very important point; since the refractive index of the gain medium increases with increasing temperature, thermal gradients will tend to focus the beam and hence promote filaments formation and beam instability. Thermal control is achieved with a Peltier element, put in contact with the copper basis where the TA is housed.

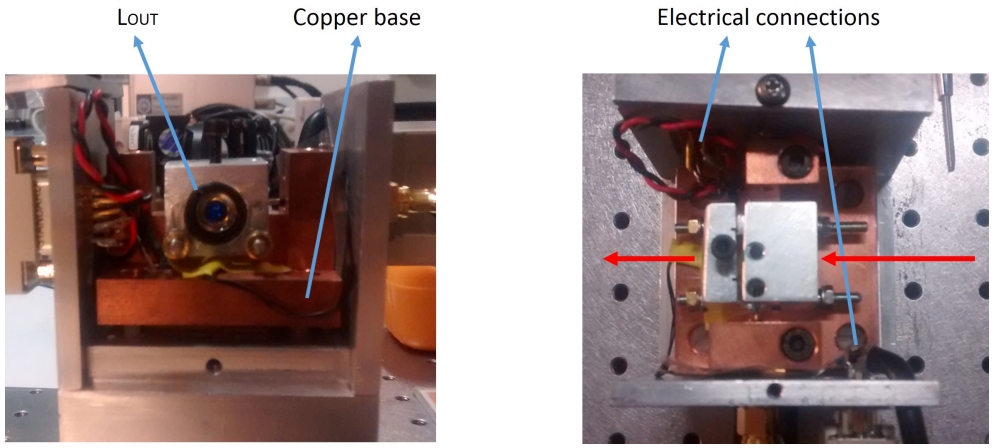

Figure 3.3: TA housing as seen from the output side (left) and from the top (right). We can see L_{OUT} and the electrical connections for the pumping current (down) and for the Peltier cell (up). The Peltier element is placed between the copper basis and the aluminium housing.

The features of the TA outgoing beam depend on several parameters. Concerning the beam shape and propagation, we can immediately notice that the beam will be elliptic. In a first approximation we can in fact consider the output facet of the TA as the focus of a beam, with waists $w_{0x,y}$ in the horizontal and vertical directions given by the dimensions of the output aperture. This will lead to different divergence angles $\theta_{x,y} = \frac{\lambda}{\pi w_{0x,y}}$ during the free-space propagation (see Fig. 3.4).

The output power of the beam, once the injection is optimized (see next section), will mostly depend on three parameters (Fig. 3.5):

- The pumping current
- The input power
- The chip temperature

In Fig. 3.5(a) we can see the output power vs. pumping current, with a threshold around 1.5A; we also see that we can reach an amplification factor of $\approx 10^3$. In Fig. 3.5(b) we can see the output power vs. input power. We see

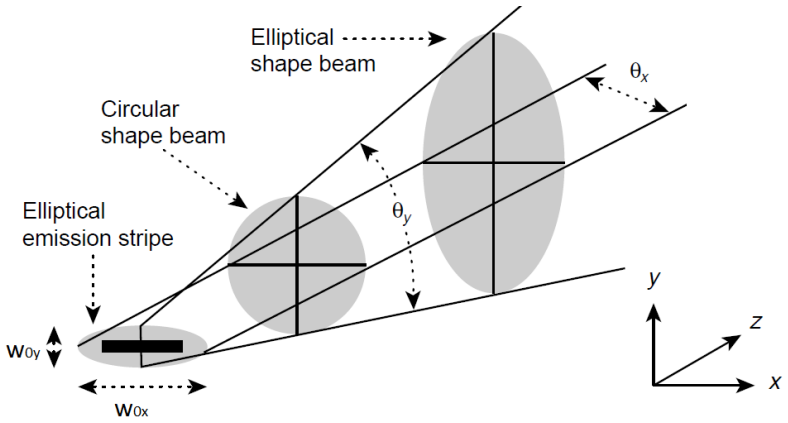

Figure 3.4: Propagation of an elliptical beam; the beam shape changes as the beam propagates.

that the output approximately grows linearly until it starts to saturate for an input power of $\approx 30mW$. In Fig. 3.5(c) the temperature dependence is shown. For a lower temperature the power slightly increases, but we cannot arbitrarily decrease the temperature since below $16 - 18^oC$ (depending on the room temperature and humidity) we get condensation of water on the cold surfaces which might damage the TA chip.

TA Injection Procedure

We describe now the procedure for optimizing the injection of the TA in order to have the highest power amplification.
We first shape properly the input beam; as we have noted before, the chip input aperture is a square of side $l \approx 3\mu m$; to optimize the input coupling we want then to focus our beam at the TA aperture with approximate waists $w_{0x,y} \leq l/2$. Since the input beam is roughly collimated we can use simplified relations for the the beam propagation through a thin lens; in our calculations we use then the relation:

$$w_0' = \frac{\lambda f}{\pi w_0} \tag{3.1}$$

where w_0 and w_0' are respectively the waist of the collimated beam before the lens and the waist of the beam at the lens focus. The telescope composed by L1 and L2 in Fig. (3.1) first expand the DL Pro beam by a factor

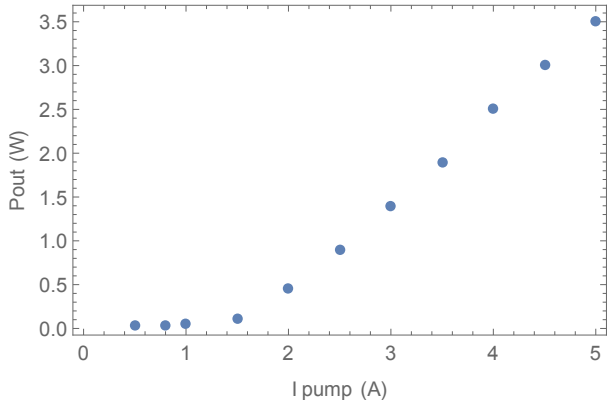

(a) Output power vs. pumping current. Input power: 32mW, TA temperature 20^oC.

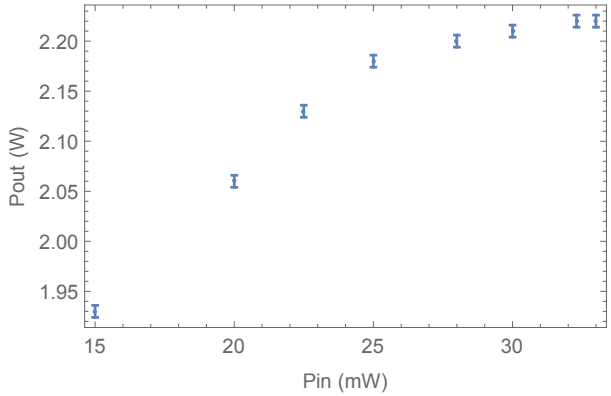

(b) Output power vs. input power. Pumping current 4.5 A, TA temperature 18^oC.

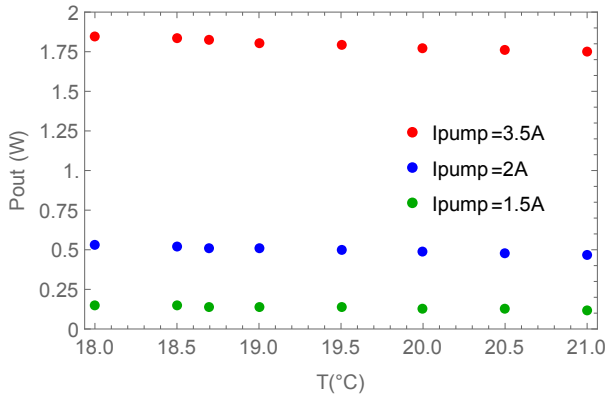

(c) Output power vs. TA temperature for various pumping currents. Input power: 30mW.

Figure 3.5: Tapered Amplifier output power dependencies.

2 ($f_1 = 50mm, f_2 = 100mm$). We choose then the input lens L_{IN} with focal length $f_{IN} = 3mm$; using equation (3.1) we calculate then a waist in the focus of $\approx 1.5\mu m$. Since the master laser beam is slightly elliptical ($w_{0x} \approx 320\mu m$, $w_{0y} \approx 230\mu m$) we expect small mismatches in the focus along horizontal and vertical directions.
To optimize the TA injection we proceed as following: we provide some current to the TA, high enough to observe the spontaneous emission of the active medium; this florescence light will be emitted both from the input and the output of the chip. What we do then is to collimate the input side florescence by placing L_{IN} at a distance $d \approx f_{IN}$ from the TA. Afterwards we adjust the vertical and the horizontal position of the lens such that the fluorescence on the input facet is not distorted or bent in horizontal or vertical direction. This requires a very precise alignment of L_{IN} on a (sub-)micrometer scale.
After this operation, we ensure a correct injection by superimposing the laser beam and the florescence. This is done via a "beam walk" with the mirrors M1 and M2: we measure the output power of the TA with a power meter and we act sequentially on M1 and M2 screws until we reach a maximum. Successively, we can slightly vary the position of L_{IN} (or equivalently slightly change the relative position of L1 and L2 to adjust the collimation) and then repeat the beam walk process, until we reach the maximum power at the TA output. Finally, a $\lambda/2$ waveplate before the TA allows to adjust the polarization of the injection beam: this is because both the emission power and the output shape will depend on it. This depends on the model; for our TA it should be p-polarized.

Beam Shaping of the Output Beam

Once optimized the injection of the TA, we want to shape the output profile in order to make it as similar as possible to a gaussian profile. This is essential for obtaining a good mode-matching at the cavity input. To achieve this we use a combination of the output lens L_{OUT} with $f_{OUT} = 4.5mm$ and the cylindrical lens CL with $f_{CL} = 50mm$. The combination of these two types of lenses is necessary to correct the beam ellipticity and astigmatism: with

the first lens we collimate the beam in the vertical direction, leaving it still expanding horizontally; the cylindrical lens will then act only on this direction. The focal lengths are chosen in order to obtain a beam approximately symmetric.
The procedure at the output has two steps: first to place L_{OUT} in order to collimate the output beam along the vertical direction, then to place CL to collimate it in the horizontal direction. Again the position of L_{OUT} has to be adjusted such that the beam is not distorted or bent in the horizontal and vertical directions. This is a crucial point since the output lens has a small diameter, and hitting the lens not in its center leads to distortion like stripes and haloes. The light outgoing from the TA has moreover a strong divergence: if the output lens is not correctly placed the beam will hit the lens edges, leading again to distortions. Immediately after the cylindrical lens we put an optical isolator to avoid back reflection on the TA chip: every eventual reflection entering the TA from the output side will be also amplified, which can lead to permanent damage.
In Figure 3.6 we report the intensity profile of the beam after the two lenses: as we can see, it has anyway a very irregular profile. This problem occurs in all tapered amplifiers, because of the inhomogeneities in the semiconductor layer and in the chip temperature, and because of nonlinear effects in the gain medium already mentioned. This, as we will see in the following, will be the principal cause of losses for coupling into a fiber.

3.1.2 Fiber Coupling

An important point for the infrared light part is the coupling of the TA amplified light into an optical fiber. This coupling is necessary mainly for two reasons: the first is that the fiber acts like a spatial filter for the beam intensity profile. A single mode fiber will in fact accept only a pure Gaussian intensity distribution, that is exactly what we want to inject into the bow-tie cavity (see section 2.5). The second reason is that the presence of the fiber will make the TA part of the set-up independent from the cavity one. As we will see in chapter 4, the alignment of the infrared light injected into the

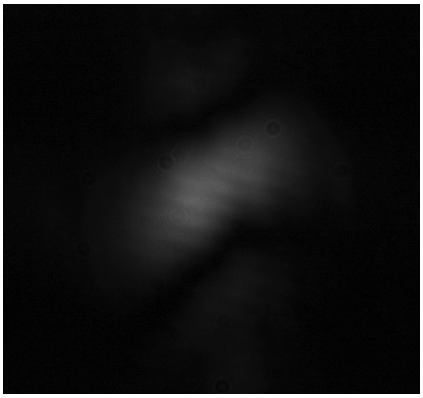

Figure 3.6: Output intensity profile after the collimation with L_{OUT} and CL for $P_{out} \sim 0.5W$. With such a beam we obtain $\sim 53\%$ coupling efficiency.

cavity is crucial. Once the fiber output collimator is fixed, we will not worry if there are misalignments before the fiber input: this will at most reduce the fiber incoupling, in which case we will only need to realign what is before the fiber input, without touching the optics on the blue light side.
We choose to use a Photonic Crystal fiber model NKT-LMA-PM-15 from NKT Photonics: this kind of fiber has a larger core diameter ($\approx 15\mu m$) with respect to an ordinary single-mode fiber (8 to $10\mu m$). This will make the coupling easier; furthermore, the fiber has a higher damage threshold at high powers. The drawback of this fiber is that the propagation mode does not have a pure Gaussian intensity distribution, but presents a typical hexagon-like shape, which reflects the internal fiber structure (Fig. 3.7).
The fiber is provided with adjustable collimators both for the input and the output side; at the input we use an "APC" ("Angled Polished Connector") type which ensures less back reflection from the fiber.

Coupling Procedure

As a first operation, we roughly couple some light into the fiber, and we adjust the position of the output collimator lens in order to obtain a collimated beam; then, we measure its waist. This operation enables us to know the waist of the fiber mode at our wavelength: with the telescope composed by the lenses L3 and L4 ($f_3 = 100\ mm, f_4 = 200\ mm$) we reduce our beam size

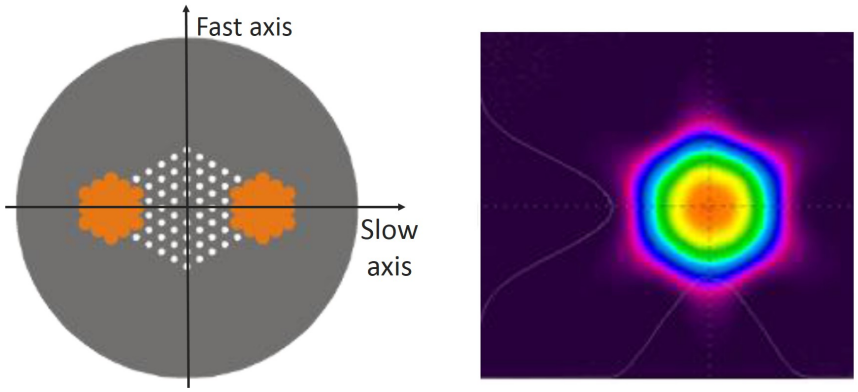

Figure 3.7: Fiber radial structure (left) and propagation mode (right). In orange we can see the "stress rods" structure for maintaining polarization.

according to this measure. Moreover, we invert the fiber, putting the side with the freshly adjusted one at the input: in this way, once we arrive at the input with the correct waist and collimation, we should in principle obtain a good coupling.

Actually the coupling is very sensitive on the beam collimation, position and angle of incidence, and the previous "by-eye" arrangements are not sufficient to guarantee the best coupling efficiency; what we do is then to follow an iterative process. For example, we slightly change the collimation in one direction by moving the cylindrical lens or L_{OUT}; then we do a beam walk on the mirror M3 and on the collimator mounting to adjust the position and the angle of the beam, and we move a bit the input collimator lens. Repeating this process we finally arrive at a maximum coupling efficiency of the order of $50-60\%$. This is a typical best value one can obtain from high-power TA chip, but it strongly depends on the individual chip and also on the power.

Optical fibers always exhibit some degree of birefringence, even if they have a circularly symmetric design, because in practice there is always some amount of mechanical stress or other effect which breaks the symmetry. As a consequence, the polarization of light propagating in the fiber gradually changes in an uncontrolled (and wavelength-dependent) way, which also depends on any bending of the fiber and on its temperature. Since we need a well defined polarization for the SHG process, the fiber we use is a polarization

maintaining fiber. This kind of fiber presents a strong built-in birefringence. Provided that the polarization of light launched into the fiber is aligned with one of the birefringent axes, this polarization state will be preserved even if the fiber is bent. We ensure that infrared light is polarized along one of the fiber axes putting a $\lambda/2$ waveplate before the input collimator, and putting at the output side another waveplate followed by a polarizing beam splitter. To align the incident polarization with one of the fiber axes we make a beam-walk with these two waveplates to minimize the power on the reflection side of the cube. In this way we maximize the extinction ratio and then minimize the ellipticity out of the fiber.

Chapter 4

Blue Light

In this chapter we describe how we build the frequency doubling cavity designed in chapter 2, and we show the locking scheme used to keep the cavity resonant with the 851nm light.

4.1 Cavity Setup

In figure 4.1 we present the complete setup scheme for the generation of the blue light, and in figure 4.2 we show a real image of it.
The cavity mirrors M2, M3, M4 are high reflectivity mirrors in the infrared ($R_H = 0.9993 \pm 0.0003$) chosen to ensure a high cavity Finesse; the incoupling mirror M1 has a reflectivity $R_1 = 0.980 \pm 0.005$ in order to match the cavity losses (see sect. 2.4). M4 is a dichroic mirror with an antireflection coating that ensures $< 5\%$ reflection for the blue. M2 is a very small mirror (6.35mm diameter, 1mm thick) in order to be piezo-actuated as fast as possible (see section 4.1.1).
Let us discuss now how we couple the output light from the fiber into the cavity. With the lens L1 we modify the beam in order to match it to the cavity mode found in section 2.1. As we have seen, the cavity mode has one focus between the planar mirrors and one in the middle of the spherical ones, and we calculated the waists for both of them. As we see from Figure 4.1, the incoupling takes place at the planar mirror arm: with the lens L1 we focus

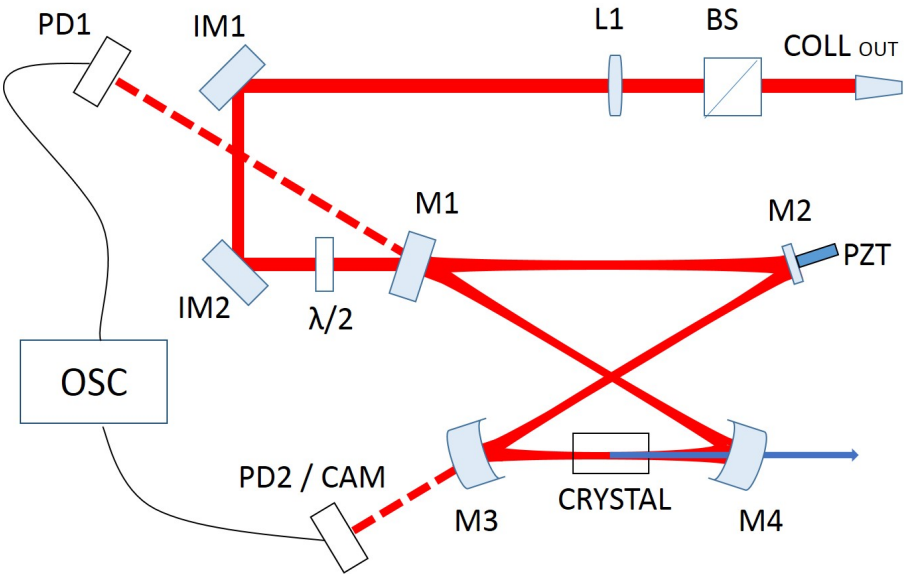

Figure 4.1: Detailed cavity setup. PD: photodiode; PZT: piezoelectric translator; OSC: oscilloscope; CAM: camera. See main text for details. The feedback part of the setup is shown in section 4.1.1.

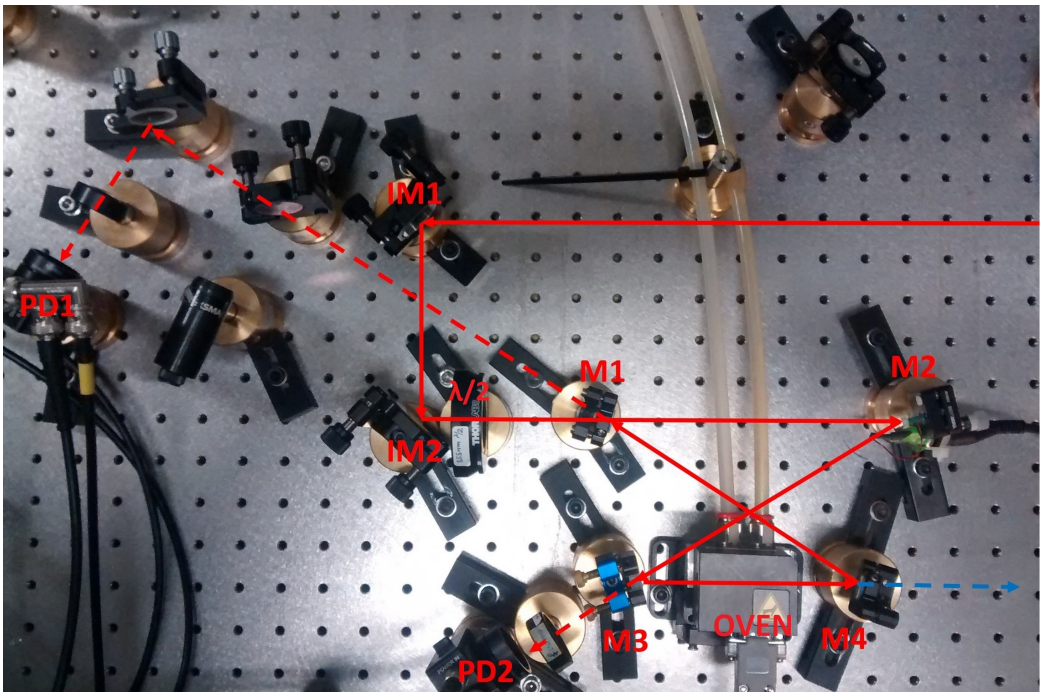

Figure 4.2: Real image of the cavity section of the setup.

the beam into the planar mirrors arm center, obtaining at the focus the waist calculated in our simulations. This allows to optimize the mode matching. The cavity beam shape is indeed essentially independent from the one of the incoming beam, since it is defined only by the distance between the mirrors, by their radius of curvature and by the crystal properties. If we inject a beam with a different waist and focus position, only a fraction of it will be resonant within the cavity. The Gauss-Hermite modes of the cavity define in fact a proper complete basis (sect. 2.5); if we inject a random beam in the cavity, only its projections on the cavity modes are allowed to resonate. We calculate then what is the best lens to use, choosing a focal length of 1000 mm. The incoupling mirrors IM1 and IM2 ensure the beam to enter the cavity with the correct angle; we set their position and angles before we mount the cavity by making the beam propagate parallel to the table surface and edges. We place then the cavity mirrors following the design described in section 2.1, ensuring the beam to hit each of them in the center. As already discussed in Chapter 2, the cavity properties are very sensitive to variations in the distance between the spherical mirrors. For this reason the mirror M4 mounting has a micrometric screw which allows to vary finely tune position.

Cavity Alignment

The cavity alignment is initially achieved without the crystal and with the help of a camera placed behind the spherical mirror M3 (see Figure 4.1), which collects the light transmitted through it. When the cavity is not properly aligned and the beam inside of it is not resonating, we see on the camera one spot corresponding to the sole transmission of the first reflection from M2. Acting on the screws of the cavity mirrors we align the beam in order to superimpose the successive round trips; when this starts to happen we see appearing on the camera the interference of the various beam round trips. Optimizing the alignment, we make the beam resonate gradually in lower order modes until we see on the camera the fundamental TEM_{00} mode. Since the cavity is not yet locked, any small vibration will modify the mirrors alignment and positions without any compensation, perturbing then the cavity

mode. At this stage we can't see thus the TEM_{00} mode alone, but we always see a succession of different modes alternating on the camera. In figure 4.3 we report a collection of camera frames showing 12 different cavity modes.

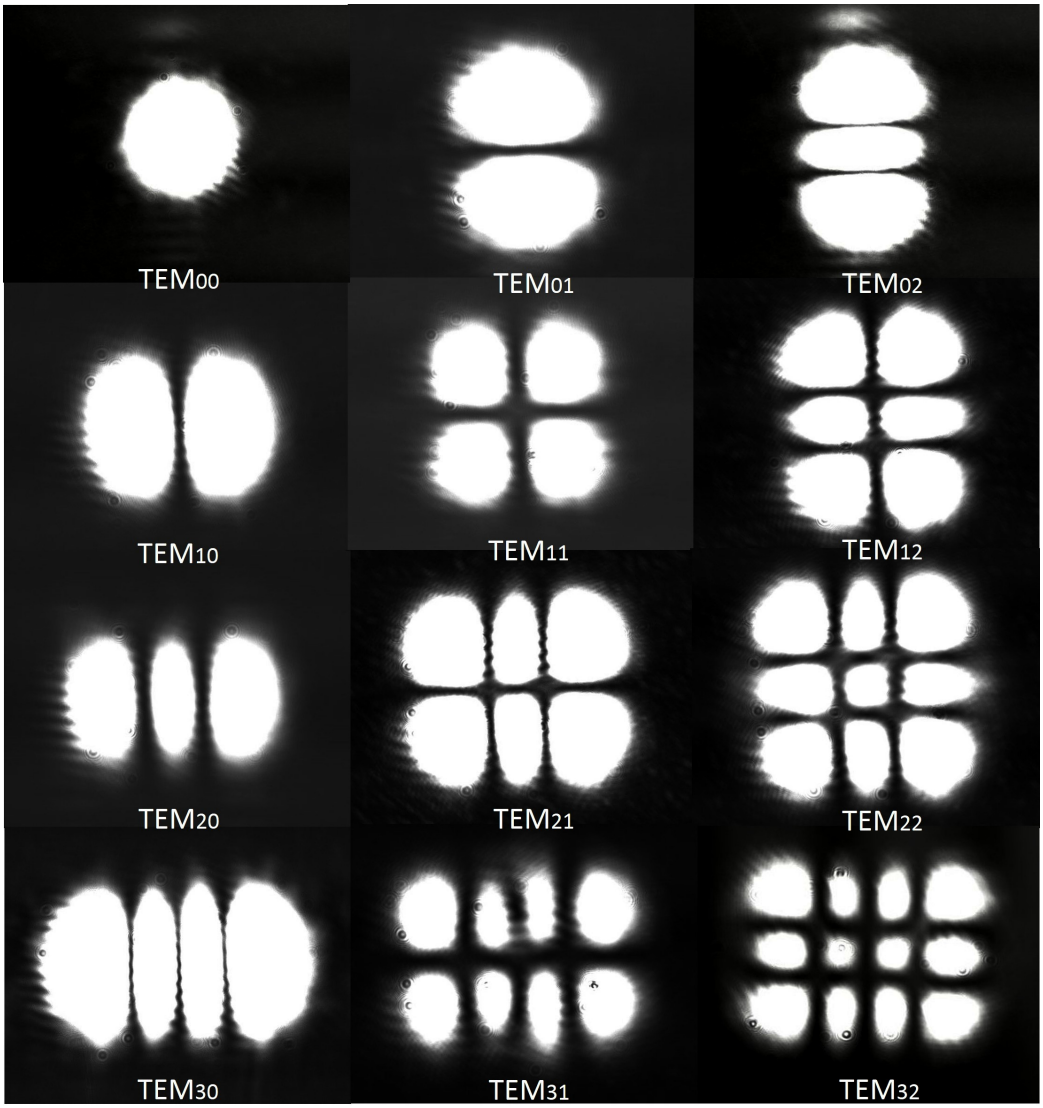

Figure 4.3: Cavity Gauss-Hermite modes. The camera is saturated in correspondence of the bright lobes; different frames are taken with slightly different zooms.

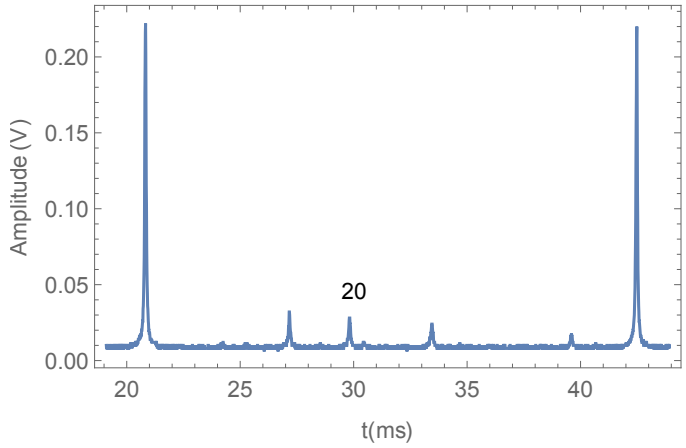

Figure 4.4: An example of cavity spectrum (one FSR) as seen on the oscilloscope after aligning the mirrors while looking at the camera.

The operations described above are useful to get the cavity roughly aligned. Further improvements are achieved replacing the camera with the photodiode PD2 and observing the transmitted cavity spectrum on the digital oscilloscope[1]. For this purpose we send a voltage ramp (10 to 20 V, 50 to 100 Hz scanning frequency) to the piezoelectric translator (PZT in figure 4.1). The mirror M2 is glued on top of it, so it will move back and forth during the piezo motion, modifying periodically the cavity length. Triggering the oscilloscope to the piezo ramp we observe then the sequence of cavity peaks. We will give a detailed analysis of the cavity spectrum in section 5.1; for the moment we report in Figure 4.4 an example of the cavity spectrum for one free spectral range as it appears after the coarse alignment done with the camera. We can see the presence of several peaks: the highest two correspond to the TEM_{00} mode: if the cavity was perfectly injected and aligned, we should see only these peaks, i.e. all the incident power should be coupled to the fundamental mode. Otherwise the beam projection on the cavity Gauss-Hermite basis will present non-zero higher order components; the heights of the peaks represent the coefficients of this decomposition.

[1]The camera can still be used for reference, placing it after the mirror M4. This position is not the optimal one when blue light begins to appear, because it is almost totally transmitted and often saturates the camera.

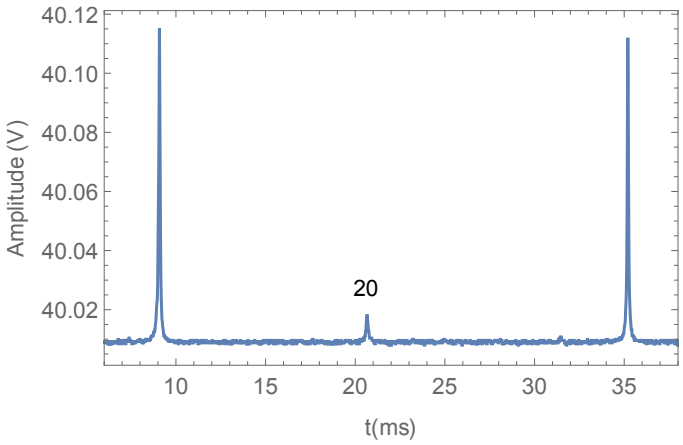

Figure 4.5: Cavity spectrum on the oscilloscope obtained reducing the height of other peaks acting on the incoupling mirrors and on the lens position. We can see still the presence of one peak, meaning that the incoupling lens does not perfectly match the beam waist inside the cavity.

The photodiode signal tells us not only what is the status of the coupling efficiency, but also gives us some indications on how to optimize it. We can easily see acting on the mirrors IM1, IM2 that the peak intensities depend on how good is the alignment of the incident beam in the vertical and in the horizontal directions. We can transfer the power going into higher order peaks to the fundamental one acting on the mirrors screws. The peak labeled as "20" in the Figure 4.4 corresponds to the TEM_{02} mode. This mode is much more difficult to suppress: that can be an indication of a non-ideal matching of the incident beam dimension and collimation. We can reduce its height modifying the lens position. We underline the crucial role of these operations related to the fact that the blue light power scales quadratically with the infrared power: e.g. if we loose 10% of the input power in other modes, we will have no more than the 80% of the blue power we would ideally expect. We report in Figure 4.5 the optimized cavity spectrum. We can still see the presence of the TEM_{02} peak, meaning that the waist matching can still be improved.
The role of the photodiode PD1 is related to the cavity locking, as we will see later; anyway it also can be helpful for the cavity alignment. This photodiode

collects both the reflected light from the mirror M1 and the transmitted light outgoing from the cavity through the same mirror M1. If we are in resonance and perfectly matched these two components interfere destructively, leading to a dip in the observed spectrum (see figure 4.6). This can be useful to estimate how good is the coupling of the infrared light, looking how deep is the TEM_{00} dip. For a perfect injection we expect in fact to see the TEM_{00} dip reaching a value close to the zero, so we can act on the mirrors/lens in order to increase the peak depth. For the actual configuration we find an incoupling efficiency of $\sim 70 - 75\%$ (Fig 4.6). For the cavity alignment it is anyway recommended to use the photodiode PD2, which has a cleaner signal because it only collects the light resonating in the cavity, which acts as a low-pass filter with timescale given by the cavity ring-down time.

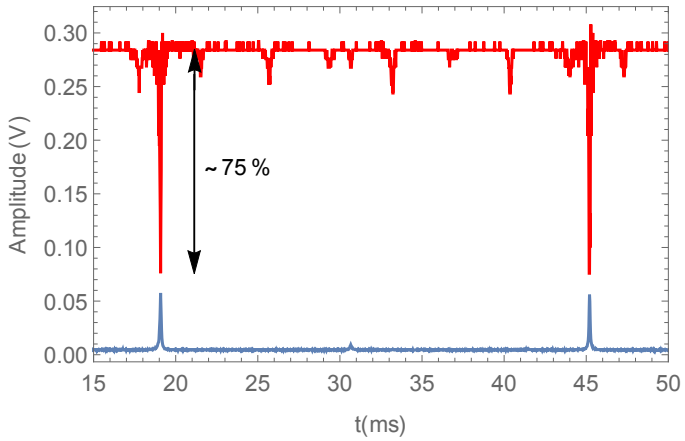

Figure 4.6: Transmission (blue) and reflection spectra (red) compared. The transmission signal is made smaller to avoid the overlap of the peaks. We can see in the reflection spectrum that the dips are not reaching the zero, suggesting that the infrared light is not perfectly coupled into the cavity. We also notice that the signal is noisier than the PD2 one, as explained in the text.

Insertion of the Crystal in the Cavity

Once the cavity has been aligned, we insert the crystal in the middle of the spherical mirrors arm. All the crystals we use are cut in a cuboidal shape, with $3mm \times 3mm$ input and output facets, and the cuboid axes don't coincide

with the crystal dielectric axes. The cutting angles in fact are chosen in order to satisfy the perfect phase matching condition for a normal incidence at the crystal facet (see sect. 1.2). The crystal is put in an oven mounted on a 5-axis translation stage. The oven will ensure the crystal to maintain the temperature for which the perfect phase matching condition is ensured; we chose this temperature to be around 20.0^oC. We insert the crystal in the cavity trying to let the infrared light propagate straight through it; in this way we get the crystal roughly aligned, and if this operation is correctly done we can see immediately some blue light "flashes", signalling that the crystal is already close to the right position. When we insert the crystal into the cavity, the spectrum on the oscilloscope changes: what we expect to see is a shift in the peaks, due to the fact that the crystal changes the cavity optical length, modifying the FSR and the mode spacing (see section 2.5). We also expect to see higher order mode peaks appearing, for the simple reason that the crystal will not be initially perfectly aligned with the cavity beam. To optimize the crystal alignment we act then on the the micrometric screws on the 5-axes translation stage, varying the crystal tilting angles until we obtain again a clean spectrum.[2]

4.1.1 Cavity Locking

At this point we proceed to get the cavity locked to the TEM_{00} peak. What we need is a feedback system which maintains the mirrors at the right distance to ensure the amplification of only the fundamental mode, correcting for any external perturbation which modifies the cavity length, allowing other modes to resonate. Such a feedback is achieved following the logic scheme of figure 4.7.

An error signal, calculated as the difference between a reference value and the output value of our system measured from PD1, is generated. The controller reads its value and sends to the system an input, varying the system output in order to minimize the error signal (such a system is called *negative feedback*

[2]Generally, once the crystal is in the cavity we need also to operate a bit again on the mirrors screws.

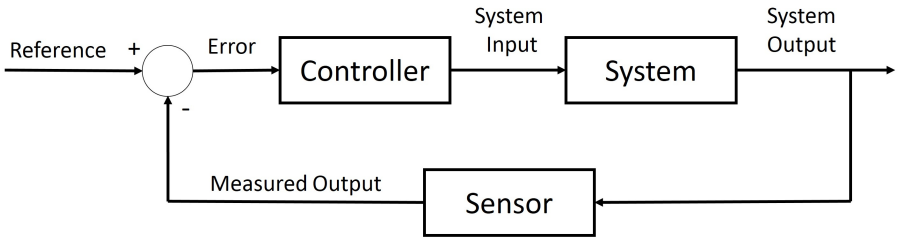

Figure 4.7: Negative feedback system logic scheme.

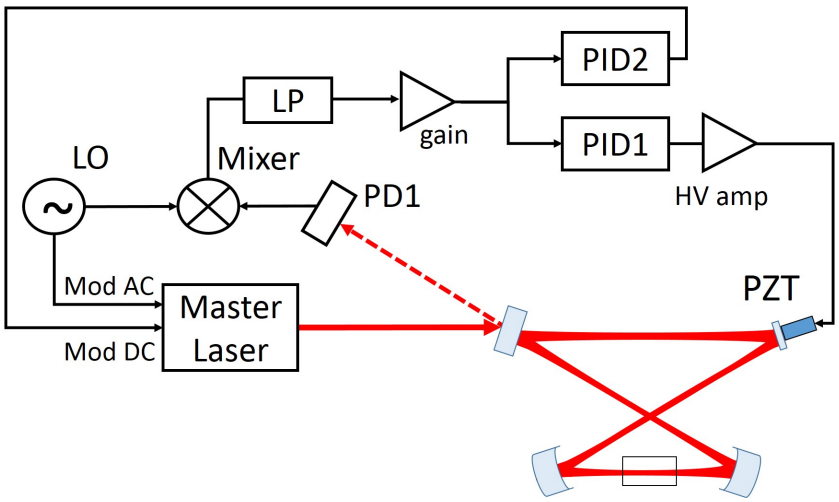

Figure 4.8: Cavity locking scheme. The local oscillator (LO) modulates the laser frequency; the light reflected from M1 is collected by PD1, whose output goes to the Mixer. The Mixer generates the error signal, which is sent to the PID controllers, which modify laser current and piezo length in order to keep the cavity locked.

system). In practice, we realize this scheme as shown in figure 4.8: the controllers we use are PID controllers, whose output is a voltage sent both to the piezo and to the master laser current, respectively. The sensor is the photodiode PD1, which collects the light reflected from the input mirror. Such a configuration is only temporary, since in a final configuration the laser will be directly locked on the Chromium spectroscopy. At the moment the master laser is free running and to "help" the piezo we give some feedback also on the current. Our error signal is generated through a Pound-Drever-Hall (PDH) scheme [47, 48, 51]. A high frequency modulation is applied to the master laser: if we consider our laser beam as monochromatic, and we

modulate it with a frequency Ω, we obtain:

$$\begin{aligned} E(t) =& E_0 e^{i(\omega_0 t + \beta sin\Omega t)} \simeq E_0 e^{i\omega_0 t}(1 + i\beta sin(\Omega t)) = \\ =& E_0(e^{i\omega_0 t} + \frac{\beta}{2} e^{i(\omega_0+\Omega)t} - \frac{\beta}{2} e^{i(\omega_0-\Omega)t}) \end{aligned} \tag{4.1}$$

where we used $\sin(\alpha) \sim \alpha$, i.e. we took a modulation with small amplitude β. Equation (4.1) describes a field composed by the original carrier frequency plus two small side-bands with frequencies $\omega_0 \pm \Omega$. When such a field is injected inside the cavity, the reflected field hitting PD1 can be written as:

$$E_{refl} = E_0(r(\omega_0)e^{i\omega_0 t} + r(\omega_0 + \Omega)\frac{\beta}{2} e^{i(\omega_0+\Omega)t} - r(\omega_0 - \Omega)\frac{\beta}{2} e^{i(\omega_0-\Omega)t}) \tag{4.2}$$

where $r(\omega)$ is the incoupling mirror reflection coefficient of the E-field. We are actually more interested in the reflected field intensity, since our photodiode is sensitive on it rather than on the field itself. The reflected intensity is given by the square modulus of Eq. (4.2):

$$\begin{aligned} I_{refl} =& |E_{refl}|^2 = E_0^2 |(r(\omega_0)|^2 + E_0^2 \frac{\beta^2}{4} \left(|r(\omega_0 + \Omega)|^2 + |r(\omega_0 - \Omega)|^2\right) + \\ &+ E_0\beta \left(Re[K(\omega_0, \Omega)]cos(\Omega t) + Im[K(\omega_0, \Omega)]sin(\Omega t)\right) + O(\Omega^2) \end{aligned} \tag{4.3}$$

where $K(\omega_0, \Omega) = r(\omega_0)r^*(\omega_0 + \Omega) - r^*(\omega_0)r(\omega_0 - \Omega)$.
The reflected intensity will thus contain several frequency components: a DC intensity, two components oscillating at the modulation frequency from the sidebands, and higher-order components from the interactions between the sidebands. We can extract then the information about the phase of the reflected field, provided that we separate one of the oscillating terms of Eq. (4.3), for example the term $\propto sin(\Omega t)$. This can be done using a mixer and a low-pass filter: the mixer will multiply I_{refl} from the photodiode with a term $sin(\Omega t)$ coming from the PDH local oscillator, resulting in a DC component and a $cos(2\Omega t)$ term. Isolating the DC component with the low-pass filter results in the Pound-Drever-Hall error signal:

$$e(\omega) = E_0\beta Im[r(\omega_0)r^*(\omega_0 + \Omega) - r^*(\omega_0)r(\omega_0 - \Omega)] \tag{4.4}$$

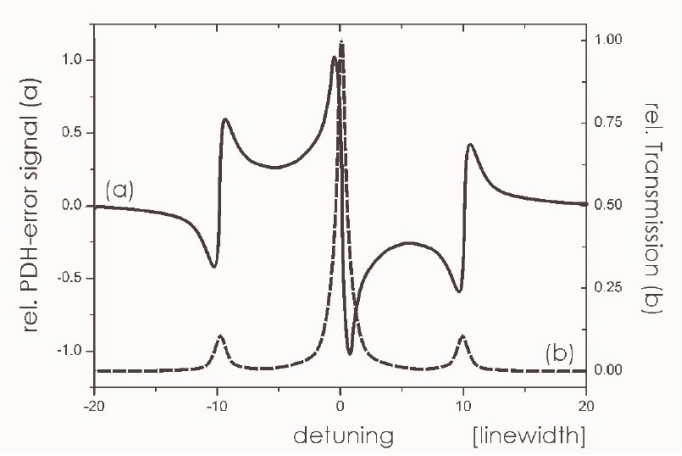

Figure 4.9: Normalized PDH error signal and modulated incident field. Picture taken from Digilock 110 manual from Toptica Photonics.

In Figure 4.9 we report a plot of $e(\omega)$ as a function of the cavity resonance frequency detuning with respect to the laser frequency, for the case in which the frequency modulation Ω is much larger than the laser linewidth $\Delta\nu$.
Such a signal is antisymmetric, and in the region of the cavity linewidth it is linear with a large slope around zero, an ideal condition for a servo loop to operate. Outside that region the signal is no longer linear, but it has still the correct sign within a frequency range of 2Ω.
Now that we have defined our error signal, the rest of the Pound-Drever-Hall technique consists of using it to adjust our system parameters in order to match the cavity mode with the laser frequency. This is achieved via a PID controller, which is a filter with adjustable proportional, integral and derivative parts. The proportional part provides fast linear negative feedback, attempting to zero the input. The integral part is used to eliminate any residual offsets that persist over longer time, i.e. it slowly corrects very small offsets which the proportional part cannot cancel out. The derivative term accounts for predicted future values of the error, based on its current rate of change, i.e. it provides the fastest responds, but is very sensitive to noise and therefore difficult to adjust. In our setup we currently do not use a D part. As we can see in Figure 4.8, our locking scheme provides the use of two PID sections, whose outputs act on the piezo and on the laser current

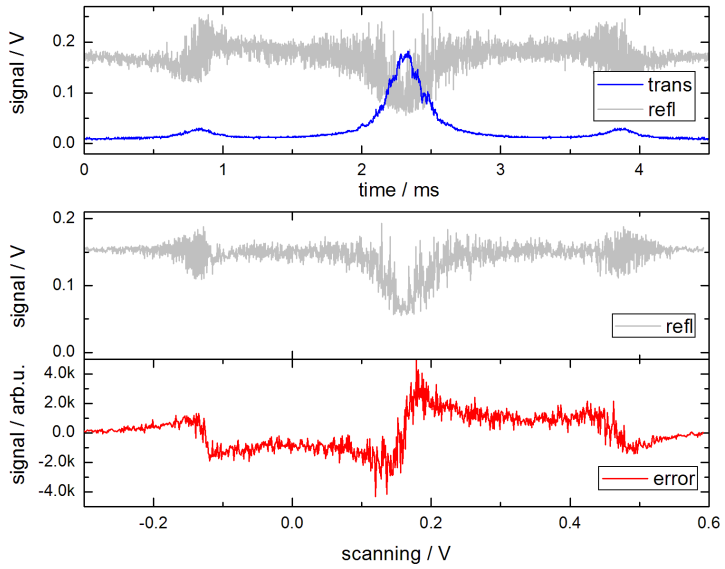

Figure 4.10: Cavity reflection (grey) and transmission (blue) signal in correspondence of the TEM_{00} peak; PDH error signal (red). We can see the presence of the sidebands. Modulation frequency: 12.5MHz.

respectively. The piezo can in fact change its position with a maximum rate of $5kHz$; to correct higher frequency noise components we act then also on the laser current.

We proceed experimentally as it follows: once we have ensured to be in a region where the master laser is single mode, we send a periodic voltage ramp to the piezo; we thus set our reference signal in correspondence with the position of the TEM_{00} peak. We engage then the PID controller, starting with low gain values and separately increasing the P and I components, in order to keep the cavity locked on the TEM_{00} mode while minimizing the noise. If we modify the cavity input power, the error signal intensity will change, so we have either to readjust the gains or to use some intensity filters to ensure always the same power on PD1. We report in figure 4.10 the error signal as it appears during the piezo scanning.

When the cavity is locked and the PIDs gains are optimized, we observe on the oscilloscope a stable signal like the one in figure 4.11, with a signal to noise ratio going from ~ 15 to ~ 3 in correspondence of noise peaks. This

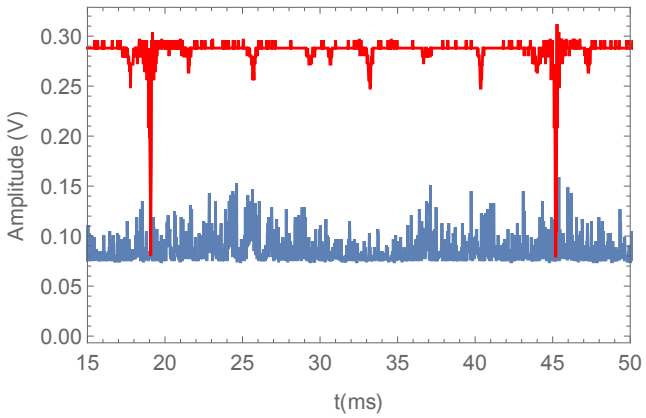

Figure 4.11: Signal on PD1 during the piezo scan (red) and for locked cavity (blue).

signal can be improved, but as we can see in figure 4.2, our cavity is directly mounted on the optical table, without any insulation from the outside. The cavity is so sensitive on external perturbation that we can see the signal oscillating if someone speaks at a distance of 2 meters. For this reason, in a final configuration the cavity will be placed in a metallic box, which could be evacuated in order to reduce acoustic noise.

We show in figure 4.12 the blue light emitted from the cavity when locked. We can see the blue beam transmitted by the dichroic mirror, and the reflected blue light that travels in the cavity, hitting the other mirrors, that partially transmit it. When the cavity is locked we can further adjust the crystal and the mirrors alignment looking directly on the blue power. In particular, we can act with a beam walk on the incoupling mirrors IM1, IM2, and we can slightly change the crystal orientation acting on the translation stage screws. We find in fact a configuration stable enough to keep the cavity locked while doing these adjustments. The same is not true for the cavity mirrors: touching their screws perturbs the cavity in a way that we loose the lock almost immediately.

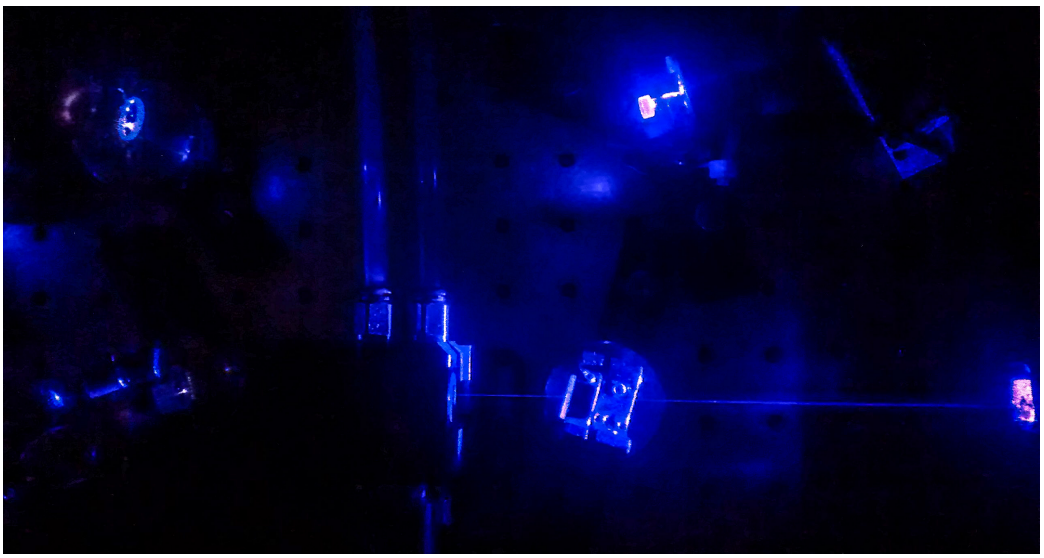

Figure 4.12: Locked cavity for 350mW measured blue power. We can see the blue beam passing through the dichroic mirror M4; we see moreover some reflected blue light hitting all the cavity mirrors.

Chapter 5

Results and Data Analysis

In this chapter we present and discuss our experimental results. We analyze first the cavity spectra. We then characterize the generated blue light, comparing all the results with the theoretical calculations outlined in chapter 2.

5.1 Cavity Spectrum Analysis

The quantities we want to measure for our aligned cavity spectra are the free spectral range, the linewidth and the finesse. We recall below the results found in chapter 2 for these parameters when the cavity is empty:

$$FSR = \frac{c}{L} \tag{5.1}$$

$$\Delta\nu = \frac{FSR}{\mathcal{F}} = \frac{c}{L}\frac{1-\sqrt{R_T}}{\pi(R_T)^{1/4}} \tag{5.2}$$

where $R_T = \prod_i R_i$ and R_i are the cavity mirrors reflectivities.
We estimate the free spectral range for our spectra using Eq. (5.1), since it depends only on the cavity length, a quantity easy to measure with a small relative error. We measure separately the mirrors relative distances with an uncertainty of 1 mm, finding for the cavity total length $L = (558 \pm 2)mm$. Thus we obtain:

$$FSR_{empty} = (537 \pm 2)MHz \tag{5.3}$$

We proceed then to measure the cavity linewidth. For this purpose we send a rectangular voltage on the piezo, which linearly and periodically changes the resonance frequency of the cavity, on the basis of what described in section 4.1.1. We detect then with the photodiode PD2 (Fig. 4.1) the transmitted light from the cavity mirror M3, which is measured on the oscilloscope as a function of the scanning time. In this way we can scan our cavity resonance frequency through the whole free spectral range or around one single peak, depending on the amplitude of the piezo ramp.
For our spectra analysis we need then to convert the oscilloscope time scale to a frequency scale. This can be done by exploiting the sidebands generated by the master laser modulation (sect. 4.1.1), which appear in the spectrum when the cavity is resonating at their frequency, and whose distance with respect to the TEM_{00} peak is 12.50MHz. Using them as a reference we can estimate the linewidth in frequency units with the simple relation

$$\Delta\nu(MHz) = \frac{\Delta\nu(s)}{\Delta side(s)} \times 12.50MHz \tag{5.4}$$

Where $\Delta\nu(s)$ is the peak FWHM in time units, and $\Delta side(s)$ is the sidebands temporal distance from the peak center (Fig. 5.1 (b)). We do not use this method for a direct measurement of FSR since the piezo scanning is not perfectly linear for the voltage range needed (15 to $20V$). Moreover, the limited oscilloscope resolution will make the peaks fit less accurate. For the evaluation of the linewidth we reduce piezo non-linearities since we scan only a small region around the TEM_{00} peak (1 to $2V$); in this way we also fully exploit the oscilloscope resolution. The ratio between the calculated FSR and the measured linewidth gives us the cavity finesse, Eq. (5.2).
We summarize in Table 5.1 the measured and the calculated cavity parameters. The peaks center positions and widths are found with Lorentzian fits. Piezo non-linearities and external perturbations can significatively alter different acquisitions, so we evaluated these quantities from several of them, taking the mean values and estimating the errors as the standard deviations. The errors for the calculated values of the finesse and of $\Delta\nu$ are estimated by evaluating Eq. (5.2) for the maximum and the minimum value of R_T compatibly with the mirrors tolerances ($R_1 = 0.980 \pm 0.005$, $R_{HR} = 0.9993 \pm 0.0003$).

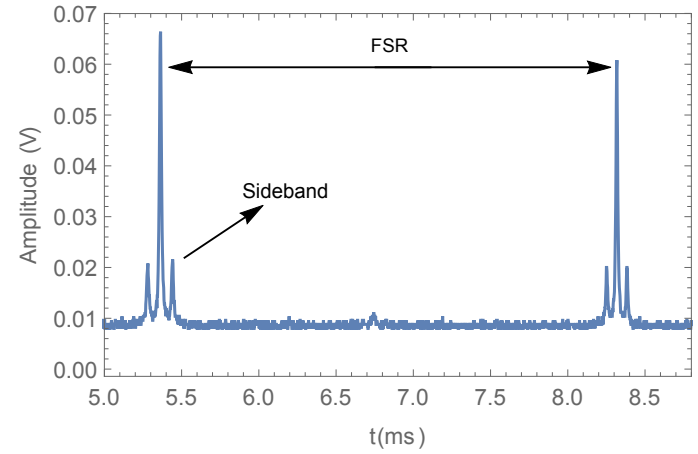

(a)

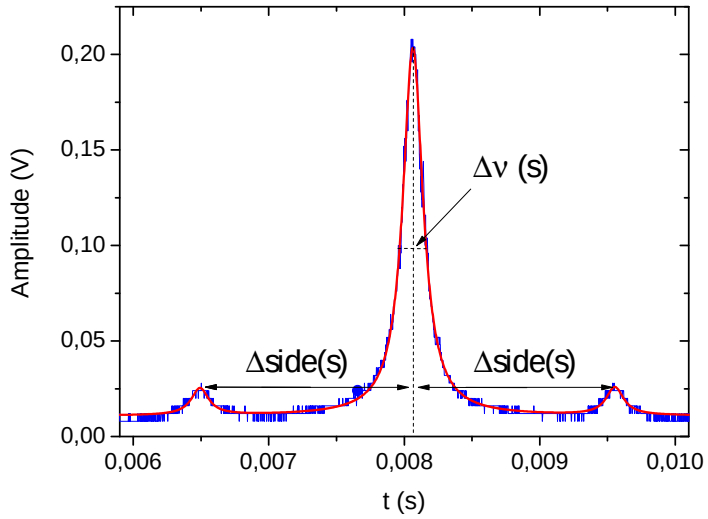

(b)

Figure 5.1: (a): scanning the piezo over one FSR. The modulation amplitude is to enhance the visibility of the sidebands: we can see the sidebands close to the TEM_{00} peaks. (b): scanning around the TEM_{00} peak to evaluate the linewidth with a lower modulation. Blue: data, red: 3 peaks Lorentzian fit. Both the picture are taken with BBO inside the cavity.

	Calculated value	Measured value
$\Delta\nu\ (MHz)$	1.9 ± 0.5	1.9 ± 0.2
$\mathcal{F}$	280^{+100}_{-60}	280 ± 30

Table 5.1: Calculated and measured values for the empty cavity.

We find a quite big error due to the critical dependence of $\mathcal{F}$ on the mirrors reflectivities. We see that all the measured values agree very well with the calculations.

LBO and BBO

The cavity parameters in the presence of the crystal change accordingly to (Sect. 2.3):

$$FSR = \frac{c}{L + l(n-1)} \tag{5.5}$$

$$\Delta\nu = \frac{FSR}{\mathcal{F}} = FSR\frac{1 - \sqrt{R_T(1-V_c)(1-\eta)}}{\pi(R_T(1-V_c)(1-\eta))^{1/4}} \tag{5.6}$$

It is useful to stress again that:

1. FSR is fixed once the crystal is in the cavity.
2. $\Delta\nu$ and $\mathcal{F}$ depend on the conversion efficiency η, thus on the power inside the cavity.

We calculate first the FSR, which is independent on the cavity power, taking again $L = (558 \pm 2)mm$ and $l_{LBO} = 15\ mm$, $l_{BBO} = 12\ mm$, $n_{BBO} = 1.610$, $n_{LBO} = 1.659$. We find:

$$\begin{aligned} FSR_{LBO} &= (528 \pm 2)MHz \\ FSR_{BBO} &= (527 \pm 2)MHz \end{aligned} \tag{5.7}$$

We evaluate then the linewidth and the cavity finesse as described for the empty cavity. We take our measurements for two different values of the

cavity input power P_{in}, in order to see if there is a variation in the finesse due to an increasing of η for high powers. Furthermore, from Eq. (5.6) we can in principle estimate the crystal total losses term $(1 - V_c)(1 - \eta)$, where we recall that V_c takes into account crystals reflections and absorption. We report in Table 5.2 the values found; we include for comparison the cavity empty measurements previously found:

	$\Delta\nu(MHz)$	$\mathcal{F}$
Empty cavity	1.9 ± 0.2	280 ± 30
LBO @ $P_{in} = 180mW$	2.2 ± 0.3	240 ± 35
LBO @ $P_{in} = 800mW$	2.2 ± 0.4	240 ± 45
BBO @ $P_{in} = 180mW$	2.3 ± 0.2	230 ± 20
BBO @ $P_{in} = 800mW$	2.2 ± 0.4	240 ± 40

Table 5.2: Measured values for the LBO linewidth, finesse and losses.

We see as expected that the finesse is higher for the empty cavity. The values obtained for the LBO and the BBO are equals within their error. We do not see moreover any variation in the cavity finesse and linewidth between low and high powers, meaning that most likely the crystal losses term is dominated by V_c in this range of powers.

5.1.1 Higher Order Modes

As we have seen in section 4.1, it is sufficient to slightly misalign the cavity incoupling mirrors to see higher order modes appearing in the spectra. We can easily isolate each one of them by scanning the piezo in a small range (1 to 2V) around each peak. In this way, looking at the camera we are able to label each of them. We report in figure 5.2 a collection of some spectra zoomed in to enlarge the higher order peaks.
We immediately notice that the transverse modes are not degenerate, i.e. that the TEM_{0y} and the TEM_{x0} modes have different frequencies. As we have noticed in section 2.5, this can be due to the fact that the cavity optical

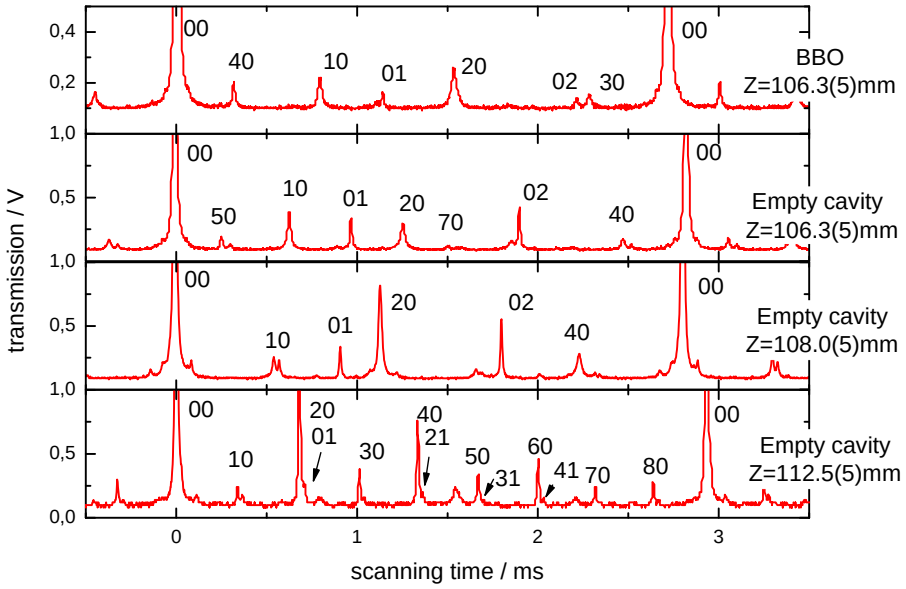

Figure 5.2: A collection of four cavity spectra with BBO crystal and for the empty cavity. The TEM_{00} peaks are truncated since the spectra are zoomed to enlarge the smaller peaks. Varying the spherical mirrors relative Z leads to different peaks spacings and positions (Eqns. (5.8), (5.9)).

path along the vertical and the horizontal direction is not exactly the same. When the crystal is inside the cavity, it might introduce an anisotropy, due to its birefringence. Anyway, we observe this effect also for the empty cavity, even if reduced. A possible reason for this behaviour can be the astigmatism introduced by the spherical mirrors when these are hit at an angle. Even though we do not know the exact reason for this observed shift we can model it easily, recalling the equations for the mode spacing and for the cavity resonance frequencies:

$$\Delta\phi = FSR\frac{\zeta(L)}{\pi} \tag{5.8}$$

$$\nu_{pmq} = \frac{c}{L+l(n-1)}\left(p+(m+q+1)\frac{\zeta(L)}{\pi}\right) \tag{5.9}$$

The TEM_{0y} "vertical" modes perfectly follow the values predicted by equations above. In contrast, the TEM_{x0} "horizontal" modes are slightly shifted from these values. If we consider that these modes acquire an additional phase shift δ during each round trip with respect to the vertical modes, their

spacing and frequencies become:

$$\Delta\phi = FSR\frac{\zeta(L)+\delta}{\pi} \tag{5.10}$$

$$\nu_{pmq} = \frac{c}{L+l(n-1)}\left(p+(m+q+1)\frac{\zeta(L)+\delta}{\pi}\right) \tag{5.11}$$

We have determined the value of δ from the spectra, and it turns out to be fairly constant around $-0.4rad$. With this value we get a perfect matching of the spectra, both for the empty cavity and for the cavity with the crystal (figure 5.3). We are still investigating about the origin of this phase shift.

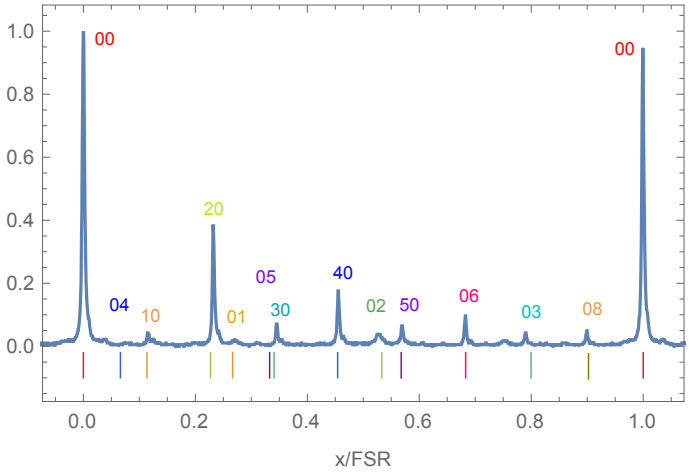

Figure 5.3: An example of observed (blue) and calculated spectrum (colored lines) for the empty cavity. We can see all the peaks matching very well.

5.2 Observed SHG efficiency

5.2.1 LBO

In figure 5.4 we report the measured blue power vs. the infrared power injected into the cavity.
The data are fitted with a function with a quadratic and a cubic term:

$$P(\omega_2) = aP^2(\omega_1) + bP^3(\omega_1) \tag{5.12}$$

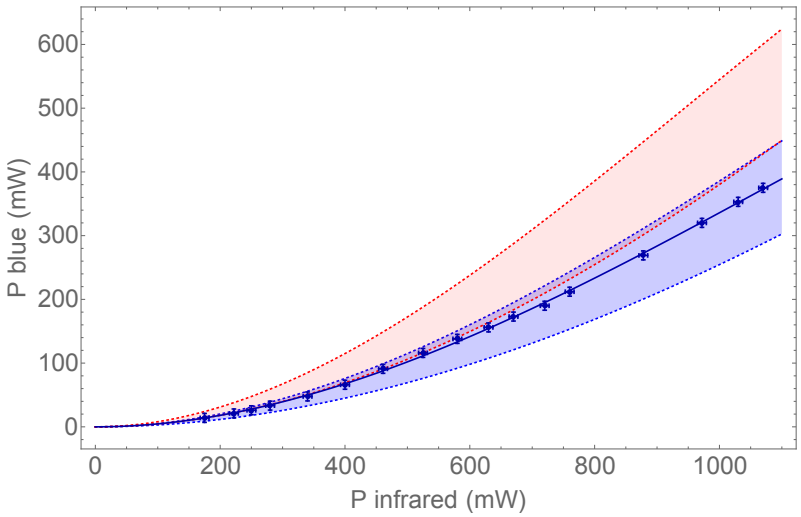

Figure 5.4: SHG power for the LBO crystal. Solid blue line: best fit to the data with fitting function Eq. (5.12). Blue shaded region: confidence interval expected considering 25% of incoupling power losses. Red shaded region: confidence region of SHG evaluated for perfect incoupling.

This can be easily understood from what we noticed in section 2.4: the SHG power does not grow quadratically with the incident infrared power as a consequence of the cavity losses. A negative cubic term describes well this behaviour. In Table 5.3 we report our best fit parameters.

Fit Function	$P(\omega_2) = aP^2(\omega_1) + bP^3(\omega_1)$
a	$(0.479 \pm 0.001)W^{-1}$
b	$(-0.143 \pm 0.007)W^{-2}$

Table 5.3: Best fit parameters for the LBO SHG efficiency.

We already noticed in section 4.1 that our incoupling is not perfect: that is signalled from the fact that the dips in the transmitted spectra do not reach the zero. From the ratio between the dip depth and the maximum value of the reflected signal we estimate the incoupling losses to be on the order of $\sim 25\%$ (see fig. 4.6). The blue shaded region in Figure 5.4 indicates the region where we expect our measured data to fall into. It is evaluated considering incoupling losses and modifying the parameters that mainly influence the

cavity power within their tolerances, like the mirrors reflectivities and the waist inside the crystal. For the waist we assume to have $w_0 = (28 \pm 2)\mu m$, considering its dependence on the spherical mirrors distance Z (figure 2.8 (c)) and assuming $Z = (108 \pm 1)mm$. The red shaded region is evaluated in the same way, but considering an ideal cavity incoupling.
We see that our data lay almost at the top of the expected region. A further improvement of the cavity incoupling is required if we want to achieve higher efficiencies. A possibility is to try different incoupling lenses/telescopes to modify the injected beam waist. We can compare our results with the one in reference [43], for which SHG is obtained with an LBO crystal for exactly the same wavelengths we use, with a similar set-up and in a smaller range of powers. In figure 5.5 we see the data are fully consistent.

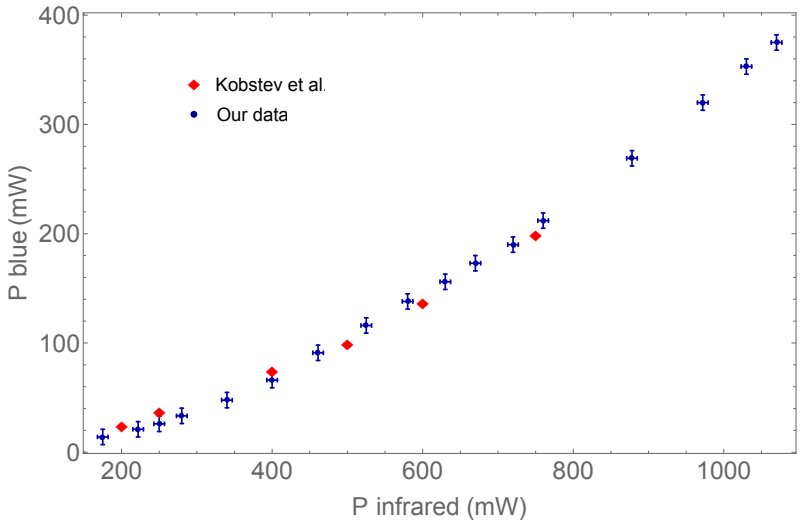

Figure 5.5: Comparison between our data and Kobstev et al. [43].

5.2.2 BBO

We report in figure 5.6 the measured blue power obtained with the BBO crystal. We followed the same procedure of previous section, considering now $w_0 = (26 \pm 2)\mu m$, $L = (557 \pm 2)mm$, $Z = (107 \pm 1)mm$.
Because of time reasons, we did not manage to optimize the cavity as well as we did for the LBO, especially for what concerns the cavity locking, so we

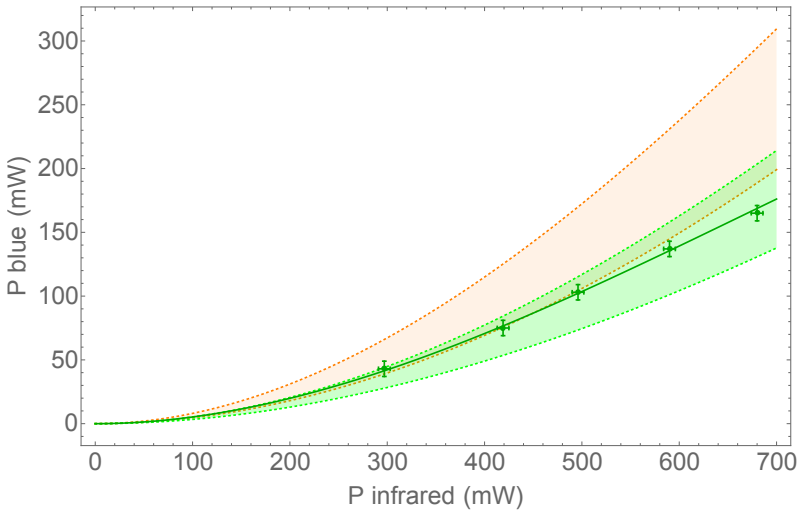

Figure 5.6: SHG power for the BBO crystal. Solid green line: best fit to the data with fitting function Eq. (5.12). Green shaded region: confidence interval expected considering 25% of incoupling power losses. Orange shaded region: confidence region of SHG evaluated for perfect incoupling.

took less data points in a smaller power region. We see anyway that our data are still at the top of the expected range up to $P_{in} \sim 600mW$, beyond which both the data and the fit seems to go to the lower limit of the expected region. The fitted curve is anyway "brought down" from the last data point, which was taken with a quite noisy signal. We thus expect that a better efficiency can be obtained by further optimizing the lock parameters for higher input powers. Below we report the BBO best fit parameters:

Fit Function	$P(\omega_2) = aP^2(\omega_1) + bP^3(\omega_1)$
a	$(0.46 \pm 0.04)W^{-1}$
b	$(-0.19 \pm 0.06)W^{-2}$

Table 5.4: Best fit parameters for the BBO SHG efficiency.

As expected from the calculation of previous sections (see Fig. 1.14 and 2.7) the generated blue power of BBO does not differ much from the one provided by the LBO crystal. We compare them in figure 5.7.

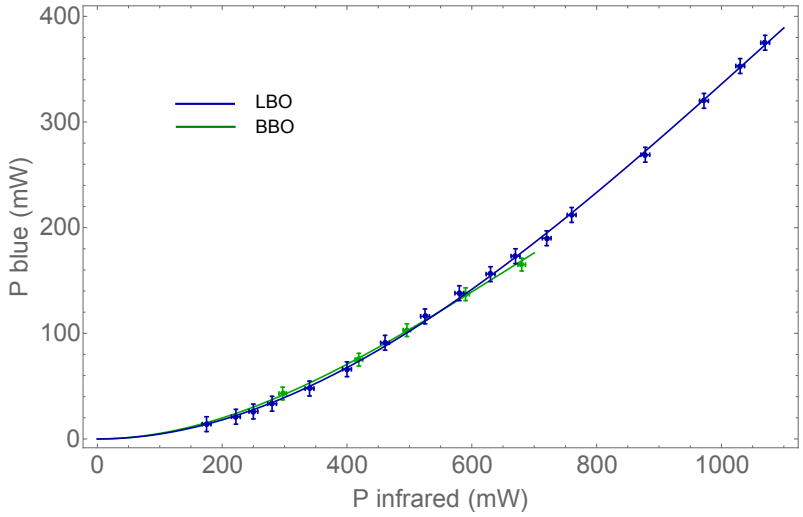

Figure 5.7: Comparison between LBO and BBO blue powers data.

5.3 Blue Light Intensity Profile

As we explained in sect. 1.2, we expect that the generated blue light beam has an elliptic shape, due to the fact that the walk off introduces a distortion in the direction of the infrared light polarization. We show in figure 5.8 a camera image of the SHG beam profile for the LBO crystal taken at $d \sim 10cm$ from the output dichroic mirror; the beam dimensions present an aspect ratio of $\sim 1/5$. Such an ellipticity has to be taken into account when we want to couple the blue light into an optical fiber. Nevertheless, this issue should be easily solvable by employing a mode matching similar to the one described in section 3.1.2.

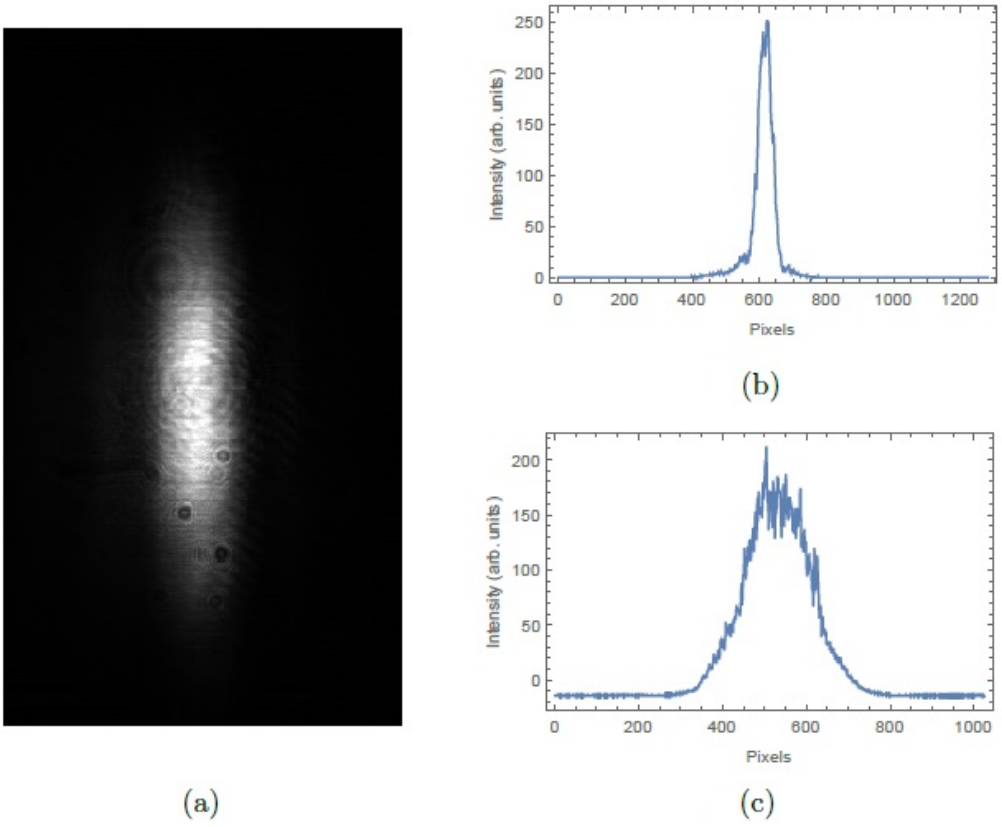

Figure 5.8: LBO blue light intensity profile. Camera frame (a); intensity distribution for the central horizontal (b) and vertical line (c).

Conclusions

The results obtained in this work, even if preliminary, confirm our understanding of the second harmonic generation process, both from a theoretical and from an experimental point of view. The observed power of the 425.5nm light is consistent with what expected from the theory and with the literature [32, 43]. Our simple setup, therefore seems a good, easy-to-handle, and unexpensive alternative to commercial systems currently employed in experiments. As future outlook, we plan to improve the infrared section of the setup, trying a Tapered Amplifier output lens of longer focal in order to make the fiber incoupling easier and more stable. On the cavity side we will optimize the beam mode matching to reduce incoupling losses and gain further SHG power. We plan then to assemble the cavity in a metallic box to isolate it better from vibrations and acoustic noise, and we will try to improve the cavity locking using a faster piezo, to correct higher frequency noise components, in a range of $\sim 20kHz$. The experiment will proceed then with the locking of the master laser to the ^{53}Cr spectroscopy. When a more stable and efficient configuration is found, we will proceed in testing of the BIBO crystal, which has a higher nonlinear coefficient than LBO and BBO and might be promising. The measurements on the BIBO will give us a complete view of the advantages and the drawbacks of BBO, LBO and BIBO crystal respectively, allowing us to choose which one to use. The last step will consist in the coupling of the blue light into a fiber, for which a shaping of the blue beam will be surely needed.

Appendix A

Here we report a simplified version of the Mathematica code we developed for the calculations of the SHG efficieny. The notation is the same used in the text. We do not report here the code for the phase matching and for the cavity design. If needed, one can use the open source program "SNLO", which provides lots of useful functions for different kinds of nonlinear processes and also for the cavity setup.

```
SpeedOfLight = 299 792 458;
Mu0 = 4 π 10^-7;
Epsilon0 = 1 / (Mu0 * SpeedOfLight^2);
goal = {Automatic, 3};
```

In[481]:=

BOYD – KLEINMANN SINGLE PASS EFFICIENCY

```
BKh[sigma_?NumericQ, beta_?NumericQ, xi_?NumericQ,
    mu_?NumericQ, kappa_?NumericQ] := Re[1/(4 xi) Exp[2 mu xi kappa]
     NIntegrate[Re[Exp[-kappa (τ0 + τ1) + i sigma (τ0 - τ1) - beta^2 (τ0 - τ1)^2] /
         ((1 + i τ0) (1 - i τ1))], {τ0, -xi (1 - mu), xi (1 + mu)}, {τ1, -xi (1 - mu),
       xi (1 + mu)}, AccuracyGoal → goal[[1]], PrecisionGoal → goal[[2]]]];
(* find optimum σ and ξ, returns {ξm,σm,hm}, β=B/√ξ (note 2),
κ=α*L/(2ξ) (note 3), α in 1/m, L in m*)
BKhmm[B_, mu_, α_, L_] := Block[{max, x, s},
    max = FindMaximum[BKh[s, B/√x, x, mu, α L / (2.0 x)], {s, 0.5, 0.6},
      {x, 1.5, 1.0}, AccuracyGoal → goal[[1]], PrecisionGoal → goal[[2]]];
    {x /. max[[2]], s /. max[[2]], max[[1]]}(*return {ξm,σm,hm}*)
   ];
BKhmm[B_] := Block[{max, x, s},
    max = FindMaximum[BKh[s, B/√x, x], {s, 0.5, 0.6},
      {x, 1.5, 1.0}, AccuracyGoal → goal[[1]], PrecisionGoal → goal[[2]]];
    {x /. max[[2]], s /. max[[2]], max[[1]]}(*return {ξm,σm,hm}*)
   ];
(* K*k1, eq. 2.20 in SI units, see Ramazza, Lechner, Masada, etc.;
λ1 in mu, n=n1=n2, deff in pm/V; *)
BKK[λ1_, n_, deff_] := 16 π^2 / (Epsilon0 SpeedOfLight λ1^3 n^2) deff^2 * 10^-6;
(* conversion efficiency, eq. 2.22, units = W*1/(W*m)*m*1 = 1;
αtot=α1+α2/2 from eq. 2.10 in 1/m and L in m; *)
BKeff[P1_, KK_, hh_, αtot_, L_] := P1 KK L hh Exp[-αtot L];
(*cavity power enhancement ϵ = Pcavity/Pin;*)
Enh[ηSHG_, Lc_, RHR_, Rin_] := (1 - Rin) / (1 - √(Rin (1 - Lc) (1 - ηSHG) RHR^3))^2;
EnhMatch[Rm_] := 1/(1 - Rm); (*for R1=Rm=(1-Lc)(1-LSHG)RHR^3*)
```

CAVITY POWER

```
(* calculate power inside cavity;*)
CavityPower[P1_, ηP1_, Lc_, RHR_] := Block[{Pc},
    Pc = If[True, (*if True analytical solution, otherwise use FindRoot*)
      (-P1 + P1 RHR^3 - Lc P1 RHR^3 + √((P1 - P1 RHR^3 + Lc P1 RHR^3)^2 +
```

```
        4 P1^2 (RHR^3 ηP1 - Lc RHR^3 ηP1))) / (2 (RHR^3 ηP1 - Lc RHR^3 ηP1)),
    Pc /. FindRoot[P1 EnhMatch[(1 - Lc) (1 - ηP1 Pc/P1) RHR^3] - Pc, {Pc, P1},
      AccuracyGoal → goal[[1]], PrecisionGoal → goal[[2]]]
   ];
  {Pc, EnhMatch[(1 - Lc) (1 - ηP1 Pc/P1) RHR^3], ηP1 Pc/P1, (1 - Lc) (1 - ηP1 Pc/P1) RHR^3}
 ];
(*same as before but does not use optimal incoupling mirror*)
CavityPower[P1_, ηP1_, Lc_, RHR_, Rin_] := Block[{Pc},
  Pc = Pc /. FindRoot[P1 Enh[ηP1 Pc/P1, Lc, RHR, Rin] - Pc,
     {Pc, P1}, AccuracyGoal → goal[[1]], PrecisionGoal → goal[[2]]];
  {Pc, Enh[ηP1 Pc/P1, Lc, RHR, Rin], ηP1 Pc/P1, (1 - Lc) (1 - ηP1 Pc/P1) RHR^3}
 ];
```

OPTIMIZED EFFICIENCY

```
(* optimize cavity for SHG;
calculation with realistic values of {LBO,BBO};
checked for LBO with Beier et.al., Apl.Phys.Lett.71, 315 (1997);*)
tmp = Block[{
   crystal = 1,
   (*input parameters*)
   ηc = 1.0(*cavity coupling efficiency*),
   RHR = 0.9993(*HR mirror reflectiviy*),
   name = {"LBO_0.1", "BBO_0.2", "BiBO_0.2"}, (*crystal name*)
   Rc = {0.2, 0.2, 0.2} 10^-2(*reflection of crystal at λ1, single surface*),
   α1 = {0.1, 0.2, 0.2}
   (*absorption coefficient of crystal at λ1 in 1/m=%/cm*),
   α2 = {0.5, 0.5, 0.5}(*absorption coefficient of crystal at λ2=
    λ1/2 in 1/m=%/cm*),
   P1 = 1(*input power in W*),
   λ1 = 0.851(*fundamental wavelength in mu*),
   n1 = {1.6098, 1.6590, 1.813}
   (*phase matched refractive index at λ1 and λ2*),
   deff = {0.777, 2.01, 3.61}(*effective nonlinear coefficient in pm/V*),
   ρ = {14.89, 65.09, 52.82}(*walkoff angle in mrad*),
   L = {15.0, 12.0, 10.0}(*crystal length in mm*),
   μ = 0.0, (*relative position of focus to center of crystal, 0=center*)
   (*optimizable parameters*)
   w0 = 31.1(*waist inside crystal in my*),
   Rin = 0.98(*incoupling mirror reflectiviy*),
   Lvar = {0, 2, 40, 2},
   (* if 3 entries vary length of crystal {start,end,step} in mm*)
   (*variables*)
   B, KK, ϵ, η, Pc, ξm, σm, hmm, α, αtot, Lc, b, info, Rm, result, hdr
```

```
},

info := Block[{},
  Print["B    = ", B];
  Print["b    = ", L / ξm,
   " mm, Rayleigh length = b/2 = ", L / (2 ξm), " mm"];
  Print["w0   = ", w0, " μm (1/e^2) = ", w0 / 2,
   " μm (σ-Gauss) = ", w0 √(2 Log[2]) , " μm (FWHM)"];
  Print["Δn   = n1-n2 = ", 2 λ1 σm / (4 π L / ξm) * 10^-3];
  Print["ξm   = ", ξm];
  Print["σm   = ", σm];
  Print["hmm  = ", hmm];
  Print["ϵ    = ", ϵ];
  Print["η    = ", η];
  Print["Rin  = ", Rin];
  Print["F    = ", π √(Rin RHR^3) / (1 - Rin RHR^3), " (w/o crystal)"];
  Print["Fc   = ", π Rin / (1 - Rin^2), " (with crystal)"];
  Print["P1   = ", P1, " W, ηc = ", ηc];
  Print["Pc   = ϵ*P1  = ", Pc,
   " W ( ΔPc/Pc = ", P1 Enh[η, Lc, RHR, Rin] / Pc - 1.0, " ) ", ϵ * P1];
  Print["P2   = η*Pc  = ", η * Pc * 1000.0, " mW"];
  Print["ηeff = P2/P1 = η*ϵ = ", η ϵ, ", ( ", η * Pc / P1, " )"];
  Print["I1 = ", 2.0 P1 / (Pi (w0 10^-4)^2), " W/cm^2, I1c = ", 2.0 Pc / (Pi (w0 10^-4)^2),
   " W/cm^2, I2 = ", 2.0 η * Pc / (Pi (w0 10^-4)^2), " W/cm^2 (inside crystal)"];
 ];
name = name[[crystal]];
Rc = Rc[[crystal]];
α1 = α1[[crystal]];
α2 = α2[[crystal]];
n1 = n1[[crystal]];
deff = deff[[crystal]];
ρ = ρ[[crystal]];
L = L[[crystal]];
P1 = ηc * P1;
B = ρ / 2 √(L 2 π / (λ1 10^-3) n1) * 10^-3;
α = α1 - α2 / 2;
αtot = α1 + α2 / 2;
Lc = 1 - (1 - Rc)^2 (1 - α1 L 10^-3);
(*single-pass crystal loss at λ1, abs+2x ref *)
(*μ=(L-2f)/L;*)
```

```
KK = BKK[λ1, n1, deff];
b = 2 π w0^2 / λ1 n1 * 10^-3;

Print["cavity efficiency for λ1 = ", λ1 * 1000.0, " nm, L = ", L, " mm:"];

ξm = L / b;
σm = 0.0;
hmm = BKh[σm, B / Sqrt[ξm], ξm, μ, 0.5 α b 10^-3];

Print["\ninput parameters:"];
η = BKeff[P1, KK, hmm, αtot, L 10^-3];
Print["ηSP  = ", ScientificForm[η], " at ", P1, " W"];
{Pc, ϵ, η, Rm} = CavityPower[P1, η, Lc, RHR, Rin];
info;

Print["\noptimized parameters:"];
(* optimize input parameters *)
{ξm, σm, hmm} = BKhmm[B, μ, α, L * 10^-3];

w0 = Sqrt[L / ξm λ1 / (2 π n1) * 10^3];

η = BKeff[P1, KK, hmm, αtot, L 10^-3];
Print["ηSP  = ", ScientificForm[η], " at ", P1, " W"];
{Pc, ϵ, η, Rin} = CavityPower[P1, η, Lc, RHR];
info;

If[Length[Lvar] == 3,
 Print["\nvary length of crystal and optimize cavity:"];
 hdr = {"L/mm", "B", "xim", "sm", "hmm", "w0/mu",
   "dn", "Pc/W", "enh", "eff", "Rin", "Pout/W", "eff_eff"};
 result = Table[Flatten[{{Lv, ρ/2 Sqrt[Lv 2 π / (λ1 10^-3) n1] * 10^-3,
       BKhmm[ρ/2 Sqrt[Lv 2 π / (λ1 10^-3) n1] * 10^-3, μ, α, Lv 10^-3]}}],
   {Lv, Lvar[[1]], Lvar[[2]], Lvar[[3]]}];
 result = Map[Join[#, {Sqrt[#[[1]] / #[[3]] λ1 / (2 π n1) * 10^3,
       2 λ1 #[[4]] / (4 π #[[1]] / #[[3]]) * 10^-3},
     CavityPower[P1, BKeff[P1, KK, #[[5]], αtot, #[[1]] 10^-3],
      1 - (1 - Rc)^2 (1 - α1 #[[1]] 10^-3), RHR]] &, result];
 result = Map[Join[#, {#[[8]] #[[10]], #[[9]] #[[10]]}] &, result];
 Print[TableForm[result, TableHeadings → {None, hdr}]];
 Print[Export[NotebookDirectory[] <> "CrystalLength_" <> name <> ".txt",
   result, "Table", TableHeadings → hdr]];

 Print[Show[
   ListPlot[result[[All, {1, 12}]], PlotStyle → {{Blue}}, PlotRange → All],
```

```
    ListPlot[result[[All, {1, 13}]], PlotStyle → {{Red}}, PlotRange → All],

    Frame → True, Axes → False,
    FrameLabel → {"L/mm", "Pout/W (blue), ηeff (red)"}, PlotRange → All
   ]];
];
result];
```

RESULTS

cavity efficiency for λ1 = 851. nm, L = 15. mm:

optimized parameters :

ηSP = 7.23728×10^{-5} at 1. W

B = 3.14356

b = 9.67405 mm, Rayleigh length = b/2 = 4.83702 mm

w0 = 28.5294 μm ($1/e^2$) = 14.2647 μm (σ-Gauss) = 33.5908 μm (FWHM)

Δn = n1-n2 = 0.000010518

ξm = 1.55054

σm = 0.75126

hmm = 0.215677

ϵ = 76.5013

η = 0.00553661

Rin = 0.986928

F = 205.888 (w/o crystal)

Fc = 119.377 (with crystal)

P1 = 1. W, ηc = 1.

Pc = ϵ*P1 = 76.5013 W (ΔPc/Pc = -4.32987×10^{-15}) 76.5013

P2 = η*Pc = 423.558 mW

ηeff = P2/P1 = η*ϵ = 0.423558, (0.423558)

I1 = 78215.7 W/cm^2, I1c = 5.9836×10^{6} W/cm^2, I2 = 33128.9 W/cm^2 (inside crystal)

Ringraziamenti

Ringrazio Matteo e il Prof. Inguscio per avermi dato la possibilità di svolgere la tesi nel loro laboratorio. Questi mesi mi hanno regalato una grande crescita professionale e personale che non dimenticherò.
Un grazie immenso ad Andreas, senza di cui sarei stato totalmente perduto! Grazie per essermi stato dietro in maniera attentissima e per avermi insegnato praticamente tutto!
Un ringraziamento particolare anche a Giovanni, per come ha seguito il mio percorso in questi anni e per la stima che ha sempre mostrato verso i miei confronti. Il Corso di Laurea adesso ha davvero un ottimo presidente!
Ringrazio poi tutti gli altri membri della BEC1 in ordine un po' sparso: Alessia (che ha condiviso con me gioie e dolori del Tapered Amplifier), Giacomone (non ti fregherò più il power meter o la cartina per l' infrarosso!), Andrea, Elettra, Francesco (fondamentali le 3 settimane in cui mi hai insegnato i trucchi per allineare la cavità!!!), Giacomo (che ancora vuole ammazzarmi perchè gli ho scaricato le pile del puntatore rosso per la fibra).
Ringrazio gli amici del Clu del Polo, con cui ho condiviso la stupenda avventura di questi anni di Università. Non scrivo i nomi perchè dimenticherei sicuramente qualcuno, ma non ce n'è bisogno perchè in cuor mio ho ben presente i loro volti (e so che è lo stesso per loro).
Da ultimo un ringraziamento alla mia famiglia, vera "roccia" a cui affidarsi, e a Carmen, il cui bene grande e gratuito è sempre fonte di stupore e di forza.

Bibliography

[1] B.E.A. Saleh, M.C. Teich, *Fundamentals of Photonics, 2nd edition*, Wiley, 2007.

[2] R.W. Boyd, *Nonlinear Optics, 3rd edition*, Academic Press, 2008.

[3] Y.R. Shen, *The Principles of Nonlinear Optics*, Wiley, 1984.

[4] W.P. Risk, T.R. Gosnell, A.V. Nurmikko, *Compact Blue-Green Lasers*, Cabridge University Press, 2003.

[5] Takeshi Fukuhara, Seiji Sugawa, and Yoshiro Takahashi Phys. Rev. A 76, 051604(R) (2007)

[6] G. Roati, F. Riboli, G. Modugno, and M. Inguscio Phys. Rev. Lett. 89, 150403 (2002)

[7] Immanuel Bloch, Jean Dalibard, and Wilhelm Zwerger Rev. Mod. Phys. 80, 885 (2008)

[8] B. DeMarco and D. Jin, Onset of Fermi degeneracy in a trapped atomic gas, Science 285, 1703 (1999).

[9]] A. G. Truscott, K. E. Strecker, W. I. McAlexander, G. B. Partridge, and R. G. Hulet, Observation of Fermi Pressure in a Gas of Trapped Atoms, Science 291, 2570 (2001).

[10] Stefano Giorgini, Lev P. Pitaevskii, and Sandro Stringari Rev. Mod. Phys. 80, 1215 (2008)

[11] Axel Griesmaier, Jrg Werner, Sven Hensler, Jrgen Stuhler, and Tilman Pfau Phys. Rev. Lett. 94, 160401 (2005)

[12] Mingwu Lu, Nathaniel Q. Burdick, Seo Ho Youn, and Benjamin L. Lev Phys. Rev. Lett. 107, 190401 (2011)

[13] S. R. Granade, M. E. Gehm, K. M. O'Hara, and J. E. Thomas Phys. Rev. Lett. 88, 120405 (2002)

[14] J. K. Chin, D. E. Miller, Y. Liu, C. Stan, W. Setiawan, C. Sanner, K. Xu, and W. Ketterle, Evidence for superfluidity of ultracold fermions in an optical lattice, Nature 443, 961 (2006).

[15] S. Ospelklaus, K. K. Ni, D. Wang, M. H. G. de Miranda, B. Neyenhuis, G. Quemener, P. Julienne, J. L. Bohn, D. S. Jin, and J. Ye, Quantum-State Controlled Chemical Reactions of Ultracold Potassium-Rubidium Molecules, Science 327, 853 (2010).

[16] M. Greiner, Optical lattices, Nature 453, 736 (2008).

[17] F. Ferlaino and R. Grimm, Forty years of Efimov physics: How a bizarre prediction turned into a hot topic, Physics 3, 9 (2010)

[18] M. H. Anderson, J. R. Ensher, M. R. Matthews, C. E. Wieman, and E. A. Cornell, Observation of Bose-Einstein Condensation in a Dilute Atomic Vapor, Science 269, 198 (1995).

[19] C. Bradley, C. Sackett, J. Tollett, and R. Hulet, Evidence of Bose-Einstein Condensation in an Atomic Gas with Attractive Interactions, Phys. Rev. Lett. 75, 1687 (1995).

[20] K. B. Davis, M. Mewes, M. R. Andrews, N. J. van Druten, D. S. Durfee, D. M. Kurn, and W. Ketterle, Bose-Einstein Condensation in a Gas of Sodium Atoms, Phys. Rev. Lett. 75, 3969 (1995).

[21] F. Schreck, G. Ferrari, K. Corwin, J. Cubizolles, L. Khaykovich, M. Mewes, and C. Salomon, Sympathetic cooling of bosonic and fermionic

lithium gases towards quantum degeneracy, Phys. Rev. A 64, 011402 (2001).

[22] A. Griesmaier, J. Werner, S. Hensler, J. Stuhler, and T. Pfau, Bose-Einstein Condensation of Chromium, Phys. Rev. Lett. 94, 160401 (2005).

[23] Q. Beaufils, R. Chicireanu, T. Zanon, B. Laburthe-Tolra, E. Marechal, L. Vernac, J.-C. Keller, and O. Gorceix, All-optical production of chromium Bose-Einstein condensates, Phys. Rev. A 77, 061601 (2008).

[24] S. Stellmer, M. K. Tey, B. Huang, R. Grimm, and F. Schreck, Bose-Einstein Condensation of Strontium, Phys. Rev. Lett. 103, 200401 (2009)

[25] Y. de Escobar, P. G. Mickelson, M. Yan, B. J. Desalvo, S. B. Nagel, and T. C. Killian, Bose-Einstein Condensation of 84Sr, Phys. Rev. Lett. 103, 200402 (2009).

[26] S. Kraft, F. Vogt, O. Appel, F. Riehle, and U. Sterr, Bose-Einstein Condensation of Alkaline Earth Atoms: 40Ca, Phys. Rev. Lett. 103, 130401 (2009).

[27] M. Lu, N. Q. Burdick, S. H. Youn, and B. L. Lev, Strongly Dipolar Bose-Einstein Condensate of Dysprosium, Phys. Rev. Lett. 107, 190401 (2011).

[28] K. Aikawa, A. Frisch, M. Mark, S. Baier, A. Rietzler, R. Grimm, and F. Ferlaino, Bose-Einstein Condensation of Erbium, Phys. Rev. Lett. 108, 210401 (2012).

[29] G. D. Boyd and D. A. Kleinman, *Parametric Interaction of Focused Gaussian Light Beams*, Journal of Applied Physics 39 (1968), 35973639, http://dx.doi.org/10.1063/1.1656831.

[30] A. Ashkin, G.D. Boyd, J.M. Dziedzic, *Resonant Optical Second Harmonic Generation and Mixing*, IEEE Journal of Quantum Electronics 2, 109 (1966).

[31] A. Ashkin, G.D. Boyd, J.M. Dziedzic, D.A. Kleinmann,*Second-Harmonic Generation of Light with Double Refraction*, Physical Review 137, 1306-1320 (1964).

[32] B. Beier, D. Woll, M. Scheidt, K.-J. Boller, and R. Wallenstein, *Second harmonic generation of the output of an AlGaAs diode oscillator amplifier system in critically phase matched LiB3O5 and β-BaB2O4*, Appl.Phys.Lett. 71 (1997), 315317.

[33] Crystal manufacturers websites: *www.lasercomponents.com, www.aphalas.com, www.coherentinc.com, www.castech.com.*

[34] P.L. Ramazza et Al. , *Second Harmonic generation from a picosecond Ti:Sa laser in LBO: conversion efficiency and spatial properties*, Applied Physics, B 75, 53-58 (2002).

[35] D.A. Roberts, *Simplified Characterization of Uniaxial and Biaxial Nonlinear Optical Crystals: a Plea for Standardization of Nomenclature and Conventions*, IEEE Journal of Quantum Electronics 28, 10 (1992).

[36] I.F. Almog, M.S. Bradley, and V. Bulovic,*The Lorentz Oscillator and its application*, MIT course (http://ocw.mit.edu/courses/electrical-engineering-and-computer-science/6-007-electromagnetic-energy-from-motors-to-lasers-spring-2011/readings/MIT6-007S11-lorentz.pdf)

[37] K.V. Diesperov, V.G. Dimitriev, A.A. Kazarov, *Specific Features of Second-Harmonic Generation in Biaxial Nonlinear-Optical Crystals*, Laser Physics Vol.6 No.6, 1040-1049, 1996.

[38] G.K. Samanta, M. Ebrahim-Zadeh, *1.2W, Tunable, Contiuous-Wave, Single-Frequency, Solid-State Blue Source*, 978-1-4244-4080 IEEE, 2009.

[39] M.J.A. Dood, *Second-harmonic generation (how to get from a wavelength of 980 to 490 nm)*,
$http://users.uj.edu.pl/\ ufdzierz/PracFot/SHG-Dood.pdf$, 2006.

[40] J.N. Walpole, *Semiconductor amplifiers and lasers with tapered gain regions*, Optical and Quantum Electronics 28 (1996), 623-645.

[41] A. Trenkwalder, *Design of a Resonator Enhanced Optical Dipole Trap for Fermionic Mixtures*, Diploma Thesis in Physics, 2007.

[42] G. Cappellini, *Development of a laser system for the encoding of qubits on degenerate Ytterbium atoms*, Diploma Thesis in Physics, 2012.

[43] S. Kobtsev, A. Zavyalov, *Efficient second-harmonic generation of CW radiation in an external optical cavity using non-linear crystal BIBO*, Proc. of SPIE Vol.6610,66100P, 2007.

[44] V. Rusleva, J. Hald, *Generation of UV light by frequency doubling in BIBO*, Optics Communications 236 (2004), 219-223.

[45] T.Freegarde,C.Zimmermann, *On the design of enhancement cavities for second harmonic generation*,Optics Communications 199(2001), 435-446.

[46] R. Grimm, M. Weidmuller, Y.B. Ovchinnikov, *Optical Dipole Traps For Neutral Atoms*, Advances in Atomic, Molecular and Optical Physics Vol. 42, 95-170 (2000).

[47] E.Black, *An introduction to Pound-Drever-Hall laser frequency stabilization*, American Journal of Physics 69 (79-87), 2001.

[48] M.Nickerson, *A review of Pound-Drever-Hall frequency locking*,

[49] L.Goldberg, D.Mehuys, *Blue light generation using a high power tapered amplifier mode-locked laser*, Applied Physics Letters 5, 522 (1994).

[50] H. Hellwig, J. Liebertz, L. Bohaty, *Exceptional large nonlinear optical coefficients in the monoclinic bismuth borate BiB_3O_6 (BIBO)*, Solid State Communications, Vol. 109, No. 4, pp. 249251, 1999.

[51] R. W. P. Drever, J. L. Hall et al., *Laser phase and frequency stabilization using an optical resonator*, Applied Physics B, June 1983, Volume 31, Issue 2, pp 97-105.